NANO · MICRO small
www.small-journal.com

# Copper-Graphene Composite (CGC) Conductors: Synthesis, Microstructure, and Electrical Performance

*Jiali Yao, Chunghwan Kim, Qiong Nian, and Wonmo Kang**

**Improving the electrical performance of copper, the most widely used electrical conductor in the world is of vital importance to the progress of key technologies, including electric vehicles, portable devices, renewable energy, and power grids. Copper-graphene composite (CGC) stands out as the most promising candidate for high-performance electrical conductor applications. This can be attributed to the superior properties of graphene fillers embedded in CGC, including excellent electrical and thermal conductivity, corrosion resistance, and high mechanical strength. This review highlights the recent progress of CGC conductors, including their fabrication processes, electrical performances, mechanisms of copper-graphene interplay, and potential applications.**

## 1. Introduction

Over the last two centuries, copper (Cu) has been the most common choice of material to power everything from the first lightbulbs and telegraphs to modern computers and home appliances. Despite its popularity, the conductivity of Cu wires has been improved by only a few percentage points compared to the International Annealed Cu Standard (IACS) established in 1914.[1] This slow technological advance in Cu-based electrical conductors becomes a major roadblock to meet ever-increasing electricity demands (e.g., consumption in the U.S. increased 13-fold from 1950 to 2021)[2] and achieve a carbon-pollution-free grid.[3] For example, a recent report[4] from the International Electrotechnical Commission estimated that Joule heating between power plants and users results in overall energy losses of up to 15% (e.g., ≈0.6 trillion kWh in the U.S. in 2021). In addition to power transmission, the efficiency of electric motors used in electric vehicles and industrial factories strongly depends on the electrical conductivity of Cu-based rotor winding,[5] e.g., 58% of energy loss in a typical electrical motor is related to Cu wires. It is worth emphasizing that >70% of the total produced energy is used by electric motors in several developed countries, including 75% in the U.S. and 80% in Canada.

J. Yao, C. Kim, Q. Nian, W. Kang
School for the Engineering of Matter, Transport, and Energy
Arizona State University
Tempe, AZ 85287, USA
E-mail: wonmo.kang@asu.edu

The ORCID identification number(s) for the author(s) of this article can be found under https://doi.org/10.1002/smll.202403241

**DOI: 10.1002/smll.202403241**

Instead of pure Cu, emerging carbon materials, such as carbon nanotubes (CNTs) and graphene (Gr), have been explored to develop effective carbon-metal composites for electrical applications. Since the discovery of Gr in 2004,[6] there have been extensive efforts to combine the attractive in-plane electrical conductivity and mechanical properties of Gr with Cu for the large-scale, cost-effective synthesis of Cu/Gr composites. The general methodology is to integrate the electrical and thermal advantages of the carbon constituents—including excellent current density limit (>$10^8$ A $cm^{-2}$), extremely high electron mobility (>15 000 $cm^2$ $V^{-1}$ $s^{-1}$), and thermal conductivity (≈5000 W $m^{-1}$ $K^{-1}$)[7–11] with Cu that offer high charge carrier density (8.491 × $10^{28}$ carriers/$m^3$ for Cu). **Table 1** compares the electrical, thermal, and mechanical properties of Gr and Cu.

Gr is a single layer of a carbon atom structure consisting of hexagonal lattice rings. Interestingly, before the discovery of Gr by the scotch tape method in 2004,[6] it was believed that 2D Gr could not exist because of thermodynamic instability.[24] In Gr, each carbon atom has four valence electrons, sharing three of them with adjacent carbon atoms to form sigma bonds and one electron through the delocalized pi bond resonance system spreading the entire plane. Because of these delocalized electrons, graphite—a nonmetal mineral consisting of multiple layers of Gr—exhibits a relatively higher electrical conductivity compared to other nonmetal materials and shares metal-like characteristics, e.g., a shiny metallic luster. Furthermore, a study from Novoselov's group[25] revealed that a single-layer Gr sheet has special electronic band structures with the Dirac point where electrons exhibit massless fermions, resulting in so-called ballistic electron transport.[26] Since these seminal works, Gr and its promising potential for electrical applications have received much attention.

Various synthesis methods of Gr have been developed, including mechanical exfoliation,[6] GO reduction,[27,28] in situ pyrolysis,[29] and chemical vapor deposition.[30] These synthesis methods, integrated with material processing techniques, such as powder metallurgy,[31] hot pressing,[32] extrusion,[33] and hot rolling,[29] push the envelope of Gr-based composite systems. However, there are only a handful of reports[29,32,34–37] where the electrical conductivities of CGC match or exceed that of pure Cu, despite the excellent electrical properties of pristine Gr.

The electrical properties of CGCs are strongly influenced by the microstructural features of Gr constituents and a Cu matrix.

 

**Table 1.** Physical properties of graphene and copper.

| Properties | | Graphene | Copper |
|---|---|---|---|
| Electrical | Electrical conductivity | 100 MS $m^{-1}$[12] | 58.1 MS $m^{-1}$[13] |
| | Electron mobility | 200 000 $cm^2 v^{-1}s^{-1}$[14] | 30–50 $cm^2v^{-1}s^{-1}$[15] |
| | Electron means free path | 28 μm[16] | 39.9 nm[13] |
| | Current density limit | 118 MA $cm^{-2}$[17] | 1 MA $cm^{-2}$[17] |
| Thermal | Thermal conductivity | 5300 W $m^{-1}K^{-1}$[18] | 401 W $m^{-1}k^{-1}$[13] |
| | Thermal expansion coefficient | −8 ppm $K^{-1}$[19] | 16.5 ppm $K^{-1}$[13] |
| | Specific heat capacity | 0.7 J $g^{-1}K^{-1}$ (graphite)[20] | 0.385 J $g^{-1}K^{-1}$[13] |
| Mechanical | Young's modulus | 1 TPa[21] | 0.117 TPa[22] |
| | Ultimate tensile strength | 130 GPa[23] | 0.22 GPa[22] |

In other words, a well-controlled assembly of Gr-Cu, including the orientation,[32] alignment,[38] spatial distribution,[39] as well as structural integrity[34] of Gr within a Cu matrix, is crucial for enhanced electrical performance of CGCs. However, it is still technically challenging to achieve a homogeneous distribution and controlled orientation of Gr. Furthermore, there are other factors that are known to lower the electrical performance of CGCs, including 1) the weak affinity at Cu/Gr interface;[30] 2) deficient consolidation of CGC,[40,41] i.e., unwanted porosity in a matrix or agglomeration of carbon materials; and 3) poor structural integrity of Gr constituents mainly due to defects formed during CGC processing.[42] In addition to these technical challenges, the exact mechanisms of Gr-dependent electrical properties of CGCs remain elusive, if not controversial.

Despite the increasing interest and promising potential of CGCs in the field of electrical applications, the currently available reviews focus mainly on the mechanical properties of metal/Gr composites[43–46] or a general overview of carbon-based conductors.[47] Indeed, a focused review on graphene-copper composites with an emphasis on their electrical applications has not been available to the best of our knowledge. This review highlights recent scientific and technical advancements in graphene-copper composite conductors with a specific emphasis on their fabrication, performance as a conductor, as well as underlying mechanisms of their enhanced properties. In this regard, this review (see **Figure 1**) first outlines the mainstream processes of engineering the CGCs, including Gr growth, Gr-dispersion methods, and consolidation techniques. Then the key material properties and the underlying mechanisms of different CGCs, including their electrical conductivity, charge-carrying capacity, and thermal/chemical stability, are reviewed and compared along with theoretical models of CGC-relevant conductors. Finally, this review ends with a brief discussion of the potential applications and future directions of CGC conductor technologies.

## 2. Fabrication of Copper-Graphene Composites

The electrical conductivity of mechanically exfoliated Gr (sheet resistivity of ≈100 Ω at high gate voltage, equivalent to ≈29.6 MS $m^{-1}$ for a single layer Gr with a thickness of 0.335 nm) was first reported by Geim and Novoselov in 2004.[6] Gr has become a promising reinforcement to conventional Cu conductors, e.g., higher electrical conductivity and greater strength-to-weight ratio. However, directly utilizing mechanical exfoliation techniques for the mass production of CGC has been difficult mainly due to both low yield and limited lateral Gr size. In this section, we review fabrication techniques for CGCs that commonly involve three steps—Gr synthesis, dispersion, and consolidation—as schematically summarized in **Figure 2**.

Gr synthesis can be done by either the breakup of graphite into smaller Gr flakes (hereafter, the top-down approach) or chemical growth of Gr on catalysts from different carbon sources (hereafter, the bottom-up approach). The top-down approach includes mechanical delamination of graphite[48,49] and chemical and/or thermal reduction of graphene oxide (GO) obtained from oxidation and delamination of graphite (often referred to as reduced graphene oxide, rGO).[39,42,50–58] For the bottom-up approach, the most common methods are in situ growth by thermal pyrolysis of organic compounds[29,31,59–66] and chemical vapor deposition (CVD).[32–34,37,67–72] The Gr dispersion in a Cu matrix is to achieve a homogeneous Cu-Gr mixture and many different techniques, as we review in great detail below, are readily available, including powder encapsulating during in situ or CVD growth of Gr,[29,31,59–62,69,70,73] mechanical mixing,[36,40,41,50–54,63–66,73–78] ball milling,[40,53,54,64,73,76] mechanical rolling,[49] electrodeposition,[48,55,57,79–81] sputtering,[37,82] and molecular level mixing.[39,42,56,58,83] It is important to note that the bottom-up approach does not require a separate dispersion step due to the direct growth of Gr on a Cu matrix, e.g., on a porous Cu foam or small-scale powders. The consolidation step, generally required regardless of the choice of prior steps, includes hot-pressing (including spark plasma sintering),[29,31,32,35,38–40,42,53–66,68–70,73,74,76,84,85] hot rolling,[29,49,51,73] hot extrusion,[33,36,61,69,72] cold rolling,[60,63,86] cold drawing,[62,66] and pressing.[75] During (or after) consolidation, CGCs are commonly annealed at high temperatures to improve Cu–Gr interfacial conditions and the conductivity of a Cu matrix.

It is important to emphasize that well-designed fabrication processes are extremely important toward improving the overall electrical performance of CGCs because each step determines the microstructural features of both Cu and Gr. Hence, this section reviews different fabrication methods of CGCs and summarizes their process-dependent microstructural features, including 1) The quality of Gr, e.g., defects density, crystalline size, and number of layers; 2) The spatial distribution and orientation of

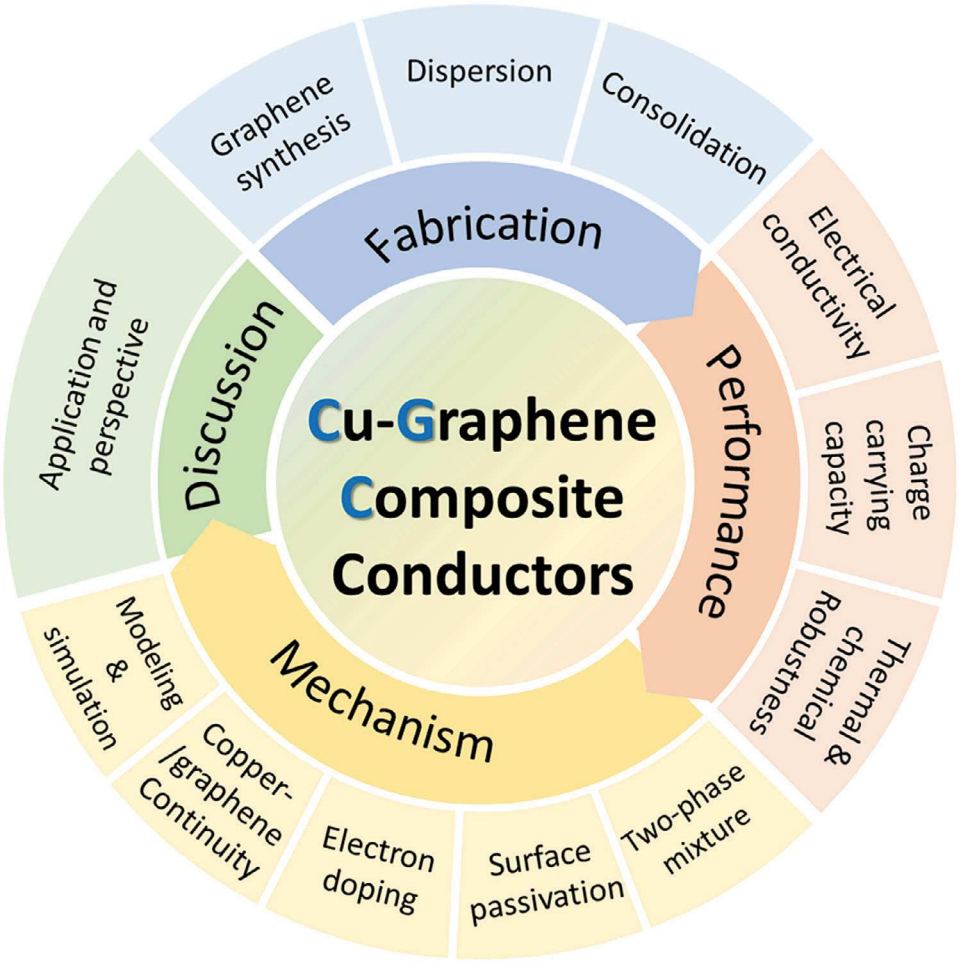


**Figure 1.** The main contents of this review, include fabrication, performance, mechanisms, and discussion of Copper-Graphene Composite (CGC) as highly effective electrical conductors.

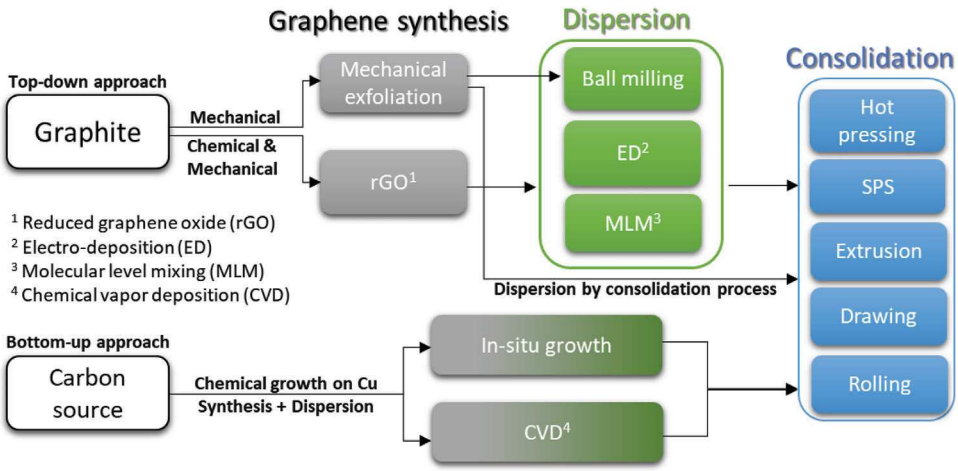


**Figure 2.** Fabrication of Cu—Gr composites (CGCs) involves Gr synthesis, dispersion, and consolidation, indicated by gray, green, and blue colors, respectively.

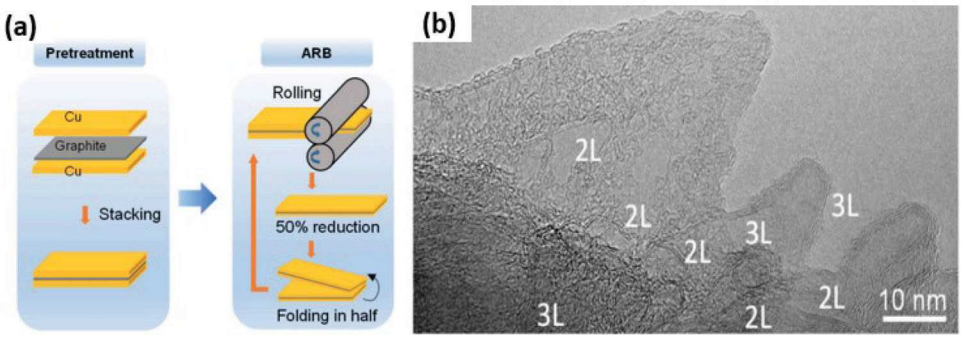


**Figure 3.** Mechanical delamination of Gr flakes from a graphite sheet. a) Schematic illustrations of (left) a graphite sheet sandwiched between thin Cu foils and (right) repeated mechanical rolling and folding, called accumulative roll-bonding (ARB), for exfoliation and dispersion of Gr flakes in Cu. b) A high-resolution transmission electron microscopic (HRTEM) image of the exfoliated Gr flakes after Cu etching from CGC after 200 ARB cycles.[49] a,b) are reproduced with permission[49] Copyright 2021, Elsevier.

reinforcement; and 3) The contact force or bonding strength between Cu and Gr reinforcement. We will revisit these microstructures in the later sections to establish a possible relationship between microstructures and the electrical properties of CGCs.

### 2.1. Graphene Synthesis and Dispersion

Highly crystalline pristine Gr exhibits superior electron mobility,[14] extremely long mean free path,[16] and unmatched electrical conductivity[12] (see Table 1). However, its electrical properties are very sensitive to defects due to its 2D nature. For example, the reported electrical conductivities of GO and rGO are in the range of $10^{-5}$–$10^{5}$ S m$^{-1}$,[28] orders of magnitude lower than that of Cu ($10^{7}$ S m$^{-1}$). Because of the highly quality-dependent electrical behavior of Gr, we present several techniques for Gr synthesis within the scope of high-performance CGCs manufacturing. In addition, the homogeneous dispersion of Gr within a Cu matrix is also crucial to fully exploit the Gr-enhanced material performance of CGC. The agglomeration of Gr in CGC is a common issue, especially at high Gr contents,[83] and it is well known that the inhomogeneous Gr distribution in CGCs limits their electrical conductivity, as well as mechanical strength. In this section, we review different Gr synthesis and dispersion techniques together because a choice of the dispersion step is often predetermined by the prior synthesis step, as schematically described in Figure 2.

#### *2.1.1. Mechanical Exfoliation*

Graphite is made up of many Gr layers that are attracted to each other by Van der Waals forces. This attraction is much weaker than that of the planar C—C covalent bonds and, as a result, individual layers can be mechanically separated by applying shear force along Gr–Gr interfaces. For example, early work[6] isolated pristine single or few-layer Gr from graphite using a so-called scotch tape technique. Obviously, the scotch tape method is time-consuming and strongly depends on the skill set of an individual. More recent studies[48,49] have improved the throughput of a mechanical exfoliation process. **Figure 3**a left shows a graphite sheet sandwiched between two thin Cu foils. This sandwiched structure repeatedly undergoes mechanical rolling and folding (see Figure 3a right) to apply shear stress between individual Gr layers. Note that repeated mechanical rolling and folding can improve a homogeneous dispersion of Gr flakes in Cu, but it is still difficult to control the exact number of Gr, as well as to maintain its lateral size (see Figure 3b). The small Gr size (<100 nm) and high defect density in Gr sheets, mainly associated with the aggressive mechanical processes, result in low electrical conductivity of CGC (i.e., 69–81% IACS).[49] Pure mechanical delamination is conceptually simple and easy to implement but suffers from limited electrical conductivity, relatively low throughput, uncontrollable thickness, and small size of Gr flakes. Because of these limitations, several chemical methods, both top-down and bottom-up, have been considered, as discussed below.

#### *2.1.2. Reduced Graphene Oxide (rGO)*

rGO is one of the popular Gr derivatives from top-down techniques. This technique utilizes chemical processes for the formation of GO and, as a result, more effectively breaks up graphite compared to pure mechanical exfoliation by applying mechanical or thermal perturbation. After achieving single or few-layer GO, chemical and/or thermal reduction of GO, as indicated by its name, is required. The modified Hummer's method[87] is commonly used to prepare GO by immersing graphite powders into acidic oxidizing agents, such as an acidified potassium permanganate solution. In this step, oxygen atoms intercalate between individual Gr layers within graphite and form oxygen-containing functional groups, such as epoxy bridge, hydroxyl, and carboxyl groups, on the surfaces and edges of individual Gr layers. These functional groups increase the distance ($D$) between individual Gr layers because the oxygen-containing functional groups and $sp^3$ carbons of GO position slightly above or below the surface of the $sp^2$ carbon plane.[88] In terms of specifics, the thickness of each GO layer is ≈1 nm (as shown in **Figure 4**a),[42] which is considerably larger than 0.34 nm for a pristine single layer Gr, leading to a volume expansion of graphite. It is important to note that interfacial delamination becomes much more effective after oxidation because of Van der Waals forces ($\propto 1/D^2$)[89] rapidly decreases for larger $D$. This is the main reason why ultrasonication[51,75] or thermal exfoliation[40] can

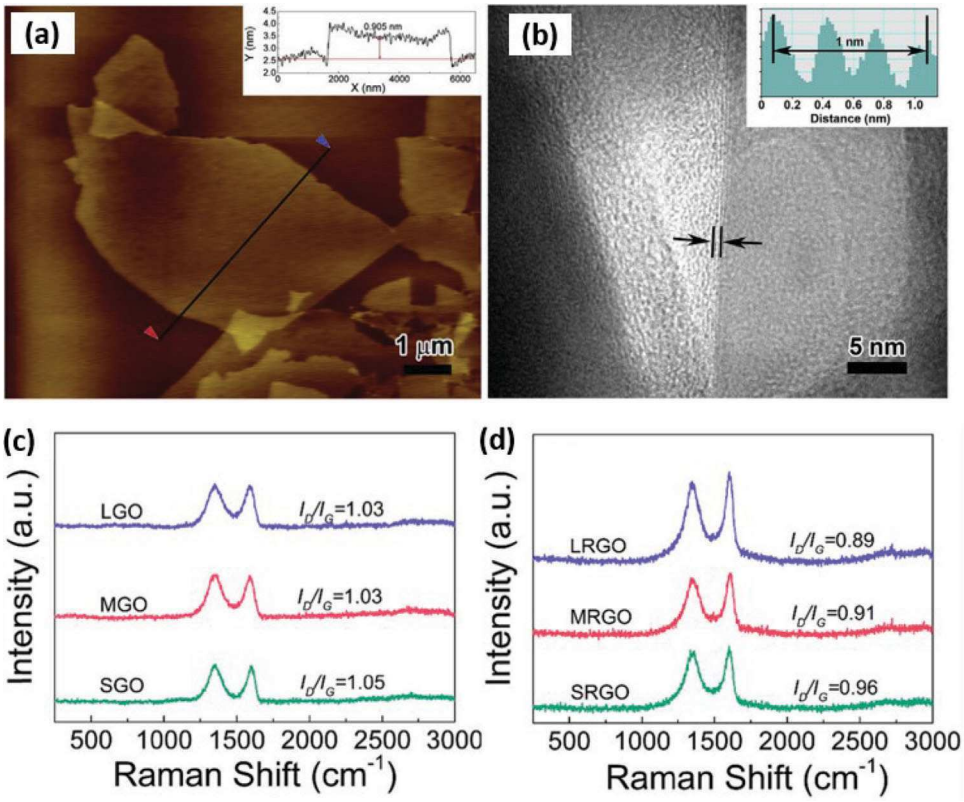


**Figure 4.** Morphology and Raman spectra of (left column) GO and (right column) rGO. a) An atomic force microscopic (AFM) image of GO flakes and b) an HRTEM image of a rGO/Cu composite after thermal reduction with hydrogen and argon.[42] c) Raman spectra of SGO (small-sized GO, lateral size ≈0.92 μm), MGO (middle-sized GO, ≈5.49 μm), and LGO (large-sized GO, ≈13.73 μm) sheets and d) after thermal reduction with hydrogen and argon of SRGO (small-sized rGO), MRGO (middle-sized rGO), and LRGO (large-sized rGO).[39] a,b) are reproduced with permission.[42] Copyright 2018, Elsevier. c,d) are reproduced with permission.[39] Copyright 2021, Elsevier.

effectively break down thick structures into single or few-layer GO structures.

The oxygen-containing functional groups help in the interfacial separation of GO but require an additional reduction step to remove the intercalated oxygen atoms and achieve high-quality rGO. For example, it has been shown that chemical and/or thermal reduction of GO increases a carbon-to-oxygen atomic ratio, e.g., from 2:1 to 33:1.[28] Here, after reduction, rGO sheets have shown reduced defect density, improved electrical conductivity, and reduced thickness (0.34 nm;[42] see Figure 4b) compared to GO. Raman analysis is frequently used for evaluating Gr quality, where the relative ratio of intensities of peaks at ≈1350 $cm^{-1}$ ($I_D$) and ≈2700 $cm^{-1}$ ($I_{2D}$) with respect to that of ≈1580 $cm^{-1}$ ($I_G$) provides information concerning defect density and number of layers, respectively.[90] A larger $I_D/I_G$ ratio indicates a higher defect density of Gr, and a higher $I_{2D}/I_G$ ratio represents a smaller number of Gr layers. Another experimental indication for the effect of reduction is shown in Figure 4c,d. The $I_D/I_G$ ratio of rGO from Raman analysis is on average 11% lower than that of GO for all different flake sizes ranging from ≈0.92 to ≈13.73 μm,[39] indicating a restoration of Gr-like atomic structure. Similarly, the atomic fraction of $sp^2$-bonded carbons in the total carbon contents of GO and rGO has been characterized, e.g., ≈29.4% for GO and 86.9% for rGO,[55] respectively, before and after thermal reduction performed at 300 °C under hydrogen and argon gases.

The electrical conductivity of rGO, while higher than GO, is still lower than pristine Gr because of residual functional groups, vacancies due to carbon monoxide/dioxide releasing during thermal reduction,[27] and other possible chemical contamination. As a result, the electrical conductivity of rGO (≈$10^5$ S $m^{-1}$)[28] is two orders of magnitude lower than the IACS (58.1 MS$m^{-1}$). Consequently, the electrical conductivity of the rGO-based CGC composites decreases as the volume fraction of rGO increases.[39,42,50–58]

The rGO-based techniques achieve the high-throughput synthesis of typically microscale rGO/GO flakes and, thus, require mechanical mixing for a homogeneous mixture of Cu and GO/rGO. For example, conventional ball milling is often utilized to mix Cu powders with commercially available GO/rGO. Note that ball milling is a time-dependent process during which Cu powders undergo cold welding, fracturing, and re-welding processes.[40] For that reason, mechanical mixing can be controlled by not only the ball-to-powder weight ratio, and the size/density of milling balls, but also the milling rate/time. Note that the use of spherical Cu powders, the most common shape in conventional powder metallurgy, causes a considerable geometric mismatch between 3D Cu powders and 2D Gr flakes. Under the strong influence of such a geometric mismatch, combined with relatively weak Cu—Gr adhesion, Gr tends to wrinkle or break on an uneven Cu surface. Regarding the geometric

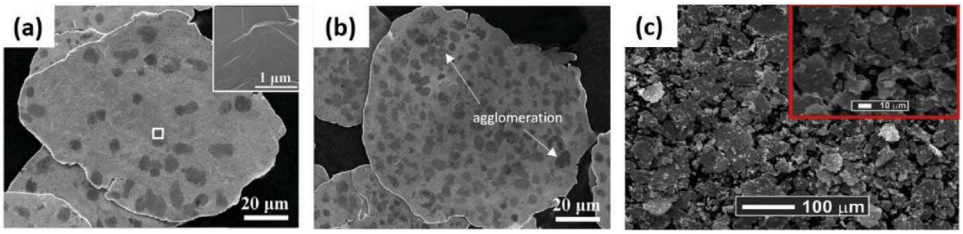


**Figure 5.** The morphology of ball-milled CGC powders. a) Scanning electron microscopic (SEM) image of 0.1 wt.% GO/Cu composite powders and b) 0.3 wt.% GO/Cu composite powders.[54] c) SEM image of 1 wt.% CGC powders formed using 4 h of milling time.[40] a,b) are reproduced with permission.[54] Copyright 2020, Elsevier. c) is reproduced with permission.[40] Copyright 2019, Elsevier.

mismatch, it is important to mention that Cu powders become flat during the early stage of the milling process,[77] as shown in **Figure** 5a,b, due to mechanical collision between ductile Cu and much harder milling balls, e.g., $ZrO_2$.[40] On the other hand, fracturing of Cu into smaller particles has been also reported, e.g., Figure 5c after 4 h of ball milling.[40]

In general, the top-down approach to synthesizing Gr compared to the bottom-up approach can achieve much higher Gr-to-Cu volume fractions. However, Cu (8.96 g $cm^{-3}$) and Gr (2.26 g $cm^{-3}$) have very different densities and weak interface affinity[30] and, as a result, agglomeration of Gr becomes unavoidable for mechanical mixing at higher Gr concentrations. Because of this, additional studies are often performed to determine the optimal Gr-to-Cu volume fraction[33,41,49,55,57,64] for high-performance CGCs. For example, Figure 5b shows more pronounced GO agglomeration at 0.3 wt.% compared to 0.1 wt.%, accompanied by the electrical conductivity deterioration, i.e., 80% IACS (0.3 wt.% GO in CGC) compared to 91% IACS (0.1 wt.% GO in CGC).

Another common method of preparing Cu—GO or Cu—rGO mixture is electrodeposition (or electroplating). Three different configurations are available: 1) depositing a Cu layer onto a Gr cathode,[81] 2) depositing a Gr layer onto a Cu electrode,[91] or 3) co-depositing Gr and Cu simultaneously onto a conductive cathode.[48,55,57] Depending on the fabrication method, 1) Soluble Cu (II) salt ($Cu^{2+}$), 2) negatively charged GO (or rGO), or 3) both are suspended in an electrolyte. Note that GO is considerably hydrophilic and carries negative charges[92] due to the oxygen-containing functional groups, such as carboxyl and hydroxyl groups, providing important characteristics to facilitate their homogeneous dispersion in electrolyte solutions. During electrodeposition, several control parameters, including applied current density, the concentration of an electrolyte, and deposition time, must be appropriately tuned to achieve precise layer thickness, Gr—to—Cu volume fraction, and Cu grain size. For example, CGCs, prepared by different electrodeposition conditions, exhibit process-dependent electrical conductivity in a range of 90–95% IACS.[48] One unique feature, compared to powder metallurgy, is that electrodeposition allows the fabrication of multi-layered Cu and Gr structures, e.g., a three-layered structure consisting of a carbon nanotube fiber, a thin Cu layer, and CVD growth Gr.[81]

Finally, molecular level mixing (MLM), developed by Hwang et al. in 2013,[83] further reduces the agglomeration of Gr. MLM shares some similarities with electrodeposition, e.g., Cu or GO can be used as a base template. But MLM relies on a chemically- or electrically-induced attractive force between Gr and Cu and, therefore, does not require any electrolysis set-up. For Cu deposition onto GO,[39,42,53,58] GO and $Cu^{2+}$ ions are suspended in an alkaline condition so that oxygen atoms on GO surfaces become active and form chemical bonds between Cu and Gr. For deposition of Gr onto Cu, cetyltrimethylammonium bromide (CTAB)[54] can be used to obtain positively charged Cu flakes. Then, Cu and GO flakes are attracted to each other due to their opposite charges and form Cu—GO bonds. MLM achieves good Cu—Gr adhesion, e.g., >200 times stronger compared to CVD-grown Gr on Cu.[83] Because of the strong adhesion, MLM-processed CGCs achieve excellent mechanical strength; for example, the tensile strength is as high as 748 MPa[42] (pure Cu: 210 MPa).[13] However, the reduction step is still required to remove oxygen atoms, e.g., in Cu—GO. In addition, the fabrication process involves multiple chemical solutions, which likely results in chemical residues and defects and, as a result, MLM-processed Cu—Gr conductors offer inferior electrical conductivities compared to pure Cu, i.e., from 62% to 94% IACS.[39,42,58]

### *2.1.3. In Situ Growth of Graphene*

In situ Gr synthesis is the bottom-up approach and involves two steps: 1) adding liquid or solid organic compounds as the carbon source within a Cu matrix and 2) then heating the mixture for the decomposition and catalytic graphitization.[29,31,59–66] Under high temperatures, as high as 900 °C,[31] organic compounds adsorbed onto the surface of Cu undergo pyrolysis and the carbon adatoms graphitize at the surface of a Cu catalyst. Use of high temperatures during in situ Gr requires careful consideration due to the relatively low melting point of Cu (1084 °C).[13] Excessive melting and localized merging of Cu powers or flakes will reduce available Cu surfaces and result in a smaller Gr—to—Cu volume fraction, as well as inhomogeneous Gr distribution. These become more relevant issues for nano-scale Cu powders/flakes because of their size-dependent melting behavior, i.e., the smaller the size and the lower the melting point.[29]

One notable approach to addressing this challenge is the use of Cu powders/small flakes uniformly coated by a thin layer of solid or viscous liquid carbon source. This method allows the separation of individual Cu powders/small flakes from each other and thus avoids unwanted merging between the powders/flakes during graphitization.[29] Two types of carbon sources are 1) solid carbon sources, such as sucrose[29] and organometallic compounds,[63,65,66] and 2) viscous liquid, such as polymethyl

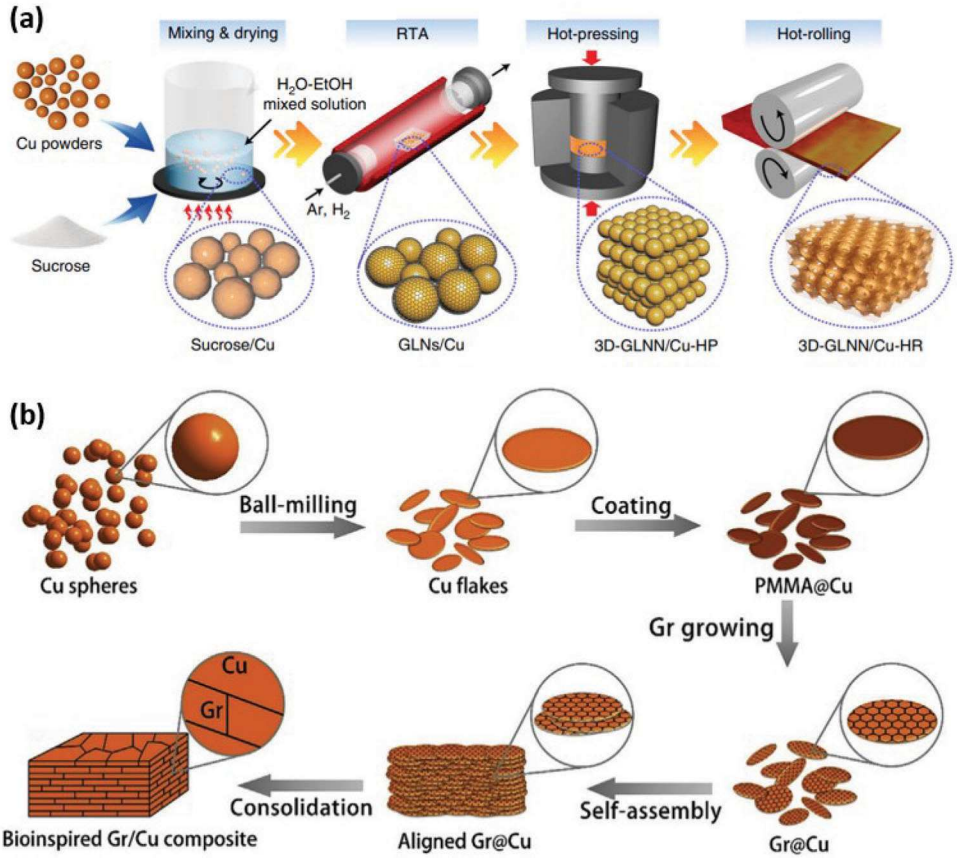


**Figure 6.** Schematic illustrations of powder metallurgy strategies involving in situ growth of Gr. a) Schematic illustration of the overall fabrication process with ordinary spherical powder metallurgy: a mixture of Cu powder and sucrose undergoes rapid thermal annealing (RTA) for in situ Gr growth. The synthesized Gr-like nanosheets on Cu powders (GLNs/Cu) are consolidated by hot pressing and subsequent hot rolling to form a 3D-Gr-like nanosheet-network/Cu composite (3D-GLNN/Cu).[29] b) Schematic illustration of the fabrication of CGC with nacre-inspired structure via flake powder metallurgy: Cu powders are first ball milled into flakes and then coated by PMMA. In situ growth of Gr and successive hot-pressing are adopted for the synthesis of the CGC with a "brick-and-mortar" structure.[38] a) is reproduced under the terms of the Creative Commons CC BY license.[29] Copyright 2020, Xiang Zhang et al. b) is reproduced with permission.[38] Copyright 2017, Elsevier.

methacrylate (PMMA),[31,73] paraffin[60,62] and naphthol.[61] Carbon structures consisting of two to ten layers of Gr have been achieved through in situ Gr growth by controlling either a type or a concentration of a carbon source. Yet, synthesizing macroscopically homogenous thin Gr structures with <5 layers remains challenging.[29,38,59]

Specifically, **Figure 6**a,b show detailed fabrication steps of CGCs based on small-scale Cu powders and flakes, respectively. In both cases, Gr-coated Cu particles undergo a consolidation process after the in situ Gr growth. During consolidation, the Gr structures are in intimate physical contact, where the Gr—Gr junctions form localized coherent lattice structures and, thus, a continuous 3D Gr network (e.g., **Figure 7**). As discussed earlier, it has been reported that such a Gr network improves the electrical conductivity of CGCs,[29] as well as their mechanical strength. Another interesting point is that the use of spherical Cu powders can cause unwanted shape changes or damage to Gr structures due to the large Cu—Gr geometry mismatch (see the rGO section for more details). To mitigate this, Cu flakes, produced by milling the spherical Cu powders, can be used as shown in Figure 6b. It has been reported that a lamellar CGC exhibits exotic mechanical and electrical properties[31] due to its nacre-like anisotropic structure. Another way to improve electrical properties is to locally alter the Cu—Gr interfacial conditions by ball milling Gr-coated Cu powders before consolidation. For example, two types of CGCs,[73] with and without the use of oxygen plasma-assisted ball milling before consolidation, were prepared by the same in situ technique. The study concluded that the former (75.5% IACS) has 5.9% higher electrical conductivity compared to the latter (71.3% IACS), although both are lower than pure Cu.

Figure 7 highlights one of the successful demonstrations of CGCs via in situ Gr syntheses where the electrical conductivity of CGC reaches 103.3% of IACS.[29] Figure 7a shows the morphology of the as-synthesized few-layer Gr (Gr-like nanosheets, GLN) covering the Cu powder matrix. Figure 7b,c show the TEM images of the Gr network after the removal of the Cu matrix from unconsolidated Gr-coated Cu powders. Figure 7c confirms that this in situ synthesis method can achieve a few-layer Gr (2-3 layers) with high crystallinity. TEM images in Figure 7d,e taken after the removal of Cu from the consolidated CGC, show the larger Gr network. Finally, the FIB-3D reconstruction image in Figure 7f

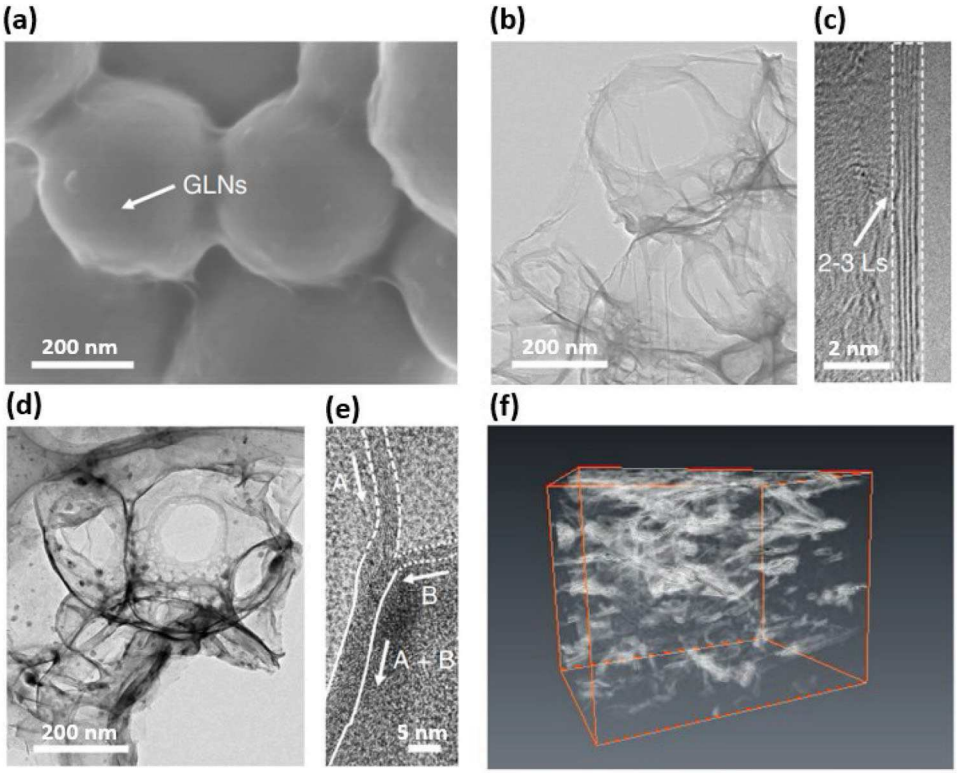


**Figure 7.** Microstructure and spatial distribution of Gr nanosheets synthesized by in situ growth. a) An SEM image of as-grown Gr-like nanosheets (GLNs) synthesized at 800 °C on Cu powders. b,c) TEM images of GLNs after etching Cu powders. d) A TEM image of the 3D Gr-like nanosheet network (3D-GLNN) after removing Cu from a hot-pressed 3D-GLNN/Cu composite. e) A HRTEM image showing the Gr-Gr junction in 3D-GLNN, where layer A and layer B merged into layer A+B. f) FIB-3D reconstruction of 3D-GLNN in a hot-pressed 3D-GLNN/Cu composite (model size:3.85 × 2.14 × 2.00 µm).[29] a–f) are reproduced under the terms of the Creative Commons CC BY license.[29] Copyright 2020, Xiang Zhang et al.

shows the Gr network extended over several micrometers. The high electrical conductivity of the CGC via *insitu* Gr synthesis is likely attributed not only to the quality of Gr layers (e.g., crystalline and contaminant) but also to the formation of the 3D Gr network that serves as a highly conductive pathway for electrical current.

### *2.1.4. Chemical Vapor Deposition (CVD) Growth of Graphene*

The electrical performance of Gr depends on both the degree of graphitization and the number of layers.[93] CVD is another bottom-up approach and has shown great potential to control these key parameters. Because of these advantages, CVD has attracted research interest to scale up the fabrication of CGC composite conductors, e.g., by assembling Gr-coated thin Cu foils or fine wires. The CVD growth of Gr on Cu, the heterogeneous catalyst, is a self-limiting surface-catalytic process[94] producing a high-quality single or bi-layer Gr film on a macroscopic Cu surface.[95] The self-limiting mechanism also limits a Gr—to—Cu volume fraction (usually within <0.1%). During CVD, a gaseous carbon source, e.g., methane,[32] ethene,[70] acetylene[67] or benzene,[34] is introduced into a heating zone together with a mixture of hydrogen and noble gases under 900–1000 °C.[73]

CVD Gr growth is versatile because it is insensitive to the geometries of a Cu substrate and type of carbon source. For example, **Figure 8** shows Raman spectra of two different Gr samples: grown by CVD on (a) Cu foils (thickness of 9–45 µm) using methane[32] and (b) Cu wires (diameter of 10–80 µm) using benzene (2–20 sccm).[34] Despite the different conditions, both results show that the excellent Gr quality, as evidenced by the absence or small magnitude of the D peak[32,34] at ≈1350 $cm^{-1}$,[96] can be achieved by tailoring CVD conditions. The CVD techniques, while the upper bound of the Gr-to-Cu volume fraction is still limited, allow more precise control of the number of Gr layers compared to other methods noted above. For example, Figure 8a shows the growth of 1–10 layers of Gr without the D peak. Similarly, Figure 8b indicates that the $I_D/I_G$ ratio strongly depends on the flow rate of carbon precursor. These studies highlight the possibility of tuning the electrical properties of CGCs by carefully tailoring key CVD parameters, i.e., temperature, pressure, growth time, the concentration of carbon precursor, etc. More details on the CVD Gr growth mechanism and the manipulation of the number of layers can be found in.[97,98]

Two successful demonstrations of CVD-processed CGC conductors are based on Gr-coated Cu foils and wires. The first example[32] is a CVD-grown single layer Gr on Cu. Despite the small volume fraction of carbon contents (as low as 0.008%), this CGC has achieved the electrical conductivity of 117% IACS, even above that of silver. The second example[34] is a CVD-grown

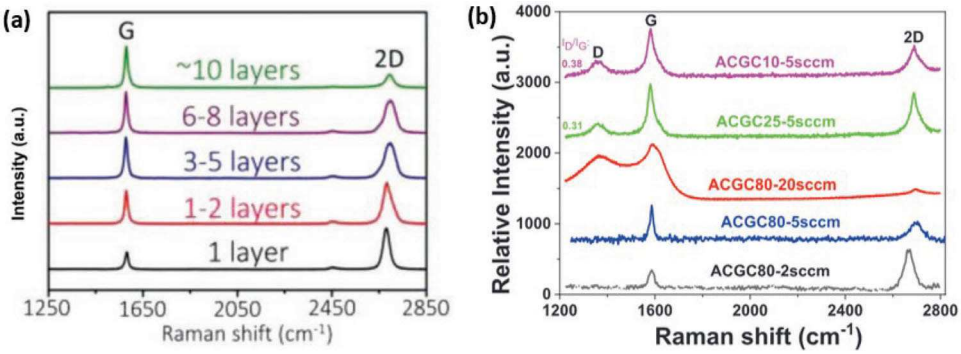


**Figure 8.** Raman spectra of CVD-grown Gr on different types of Cu catalysts: a) 1–10 layers of Gr on thin Cu foils grown by CVD with methane as the carbon source[32] and b) changes in Raman responses from Gr on fine Cu wires using different CVD conditions, i.e., (from top to bottom) 10, 25, 80, 80, 80 µm of wire diameters and 5, 5, 20, 5, 2 sccm of benzene flow rates, respectively.[34] a) is reproduced with permission.[32] Copyright 2019, John Wiley and Sons. b) is reproduced with permission.[34] Copyright 2021, John Wiley and Sons.

multilayer Gr on a 10-µm-diameter Cu wire. This work has demonstrated an impressive 41% improvement in its electrical conductivity compared to its pure Cu wire counterpart (or 123.8% IACS), the highest electrical conductivity among the reported CGCs, to the best of our knowledge.

### 2.2. Consolidation

CGC processing commonly utilizes Cu powders/flakes/foils for Gr synthesis and, therefore, a consolidation step is crucial to achieve fully compacted (or densified) macroscopic CGC conductors for their practical application. Consolidation involves often excessive compressive mechanical deformation of CGCs and this unavoidably alters their microstructures, e.g., higher dislocation densities in Cu, as well as damage and tear to Gr. Such microstructural changes negatively affect the electrical conductivity of CGC, often mitigated by performing consolidation at high temperatures.

#### *2.2.1. Hot Pressing and Spark Plasma Sintering (SPS)*

Hot pressing[29,31,32,35,40,56,60,62,63,65,66,69,70,73,84] and SPS,[39,42,53–55,57–59,64,68,74,76] owing to their technical maturity in powder metallurgy, are the most common method for CGC consolidation. Both hot pressing and SPS apply large compressive stress and high temperature to loosely packed CGC placed in a mold, typically in an inert, controlled atmosphere. The major difference between the two methods is how porous CGCs are heated: hot pressing-a mold heated by an induction coil or other external heating elements (temperature range: 800–900 °C) and SPS-the volumetric Joule heating of a conductive sample within a mold by applying electrical current (temperature range: 600–800 °C).

In general, SPS achieves more effective heating of a sample with a faster heating rate and, therefore, requires less pressing time. In terms of specifics, hot pressing, and SPS are typically performed under 30–50 MPa for 20–60 min and under 35–50 MPa for 3–20 min, respectively. Note that the temperature ranges of both methods are considerably higher than the recrystallization temperature of Cu (326 °C),[99] leading to dislocation annihilation, grain coarsening, and grain boundary rotation.[32] In addition, it is known that discrete Gr structures can merge with each other at contact points or planes[29] under high compressive stress and temperature conditions to form a continuous Gr network. One notable work[35] compares the electrical conductivities of CGCs after consolidation by hot pressing and SPS. For the former, the oxygen content in CGC was ≈16.4 ppm with 98.8% IACS. Interestingly, SPS reduced the oxygen content from 16 to 7.45 ppm and achieved 108.6% IACS. It is noteworthy that the use of high temperatures can also have negative effects because GO starts to decompose at a temperature as low as 216 °C, releasing CO and $CO_2$[100] and creating vacancies in the honeycomb structures. For example, such thermal pyrolysis of Gr structures in CGC was reported in[56] after hot pressing. Additionally, because of slow-strain-rate processing and homogeneous stress applied in the axial direction, the architecture of CGC (synthesized through a similar route as shown in Figure 6b) can be preserved during sintering, as indicated in **Figure 9**a,b. The Electron backscattered diffraction (EBSD) image along the cross-plane direction shows a much smaller average grain size than that along the in-plane direction of CGC, indicating the well-preserved "brick-and-mortar" hierarchy structure after hot pressing.

#### *2.2.2. Extrusion, Drawing and Rolling*

Mechanical consolidation methods, including extrusion, drawing, and rolling, are readily available to process macroscale CGCs, e.g. wires,[33] foils,[36] foams,[86] or blocks (hot pressed).[61,62,66,69] The choice of extrusion, drawing, and rolling is dependent on the targeted shape of the final products: extrusion for objects with fixed cross-sectional profiles, drawing for wires, and rolling for foils or plates. Among them, rolling has the highest tonnage in the metal industry,[101] so synthesis of CGC by using the rolling technique for consolidation has the highest potential for roll-to-roll mass production. Furthermore, due to the lack of affinity between Cu and Gr, especially for bottom-up powder metallurgy strategies, the density of compacted composite is always lower than their calculated theoretical density.[40,41,50–52,54,56,64,70] The existing voids within CGC would lower electrical

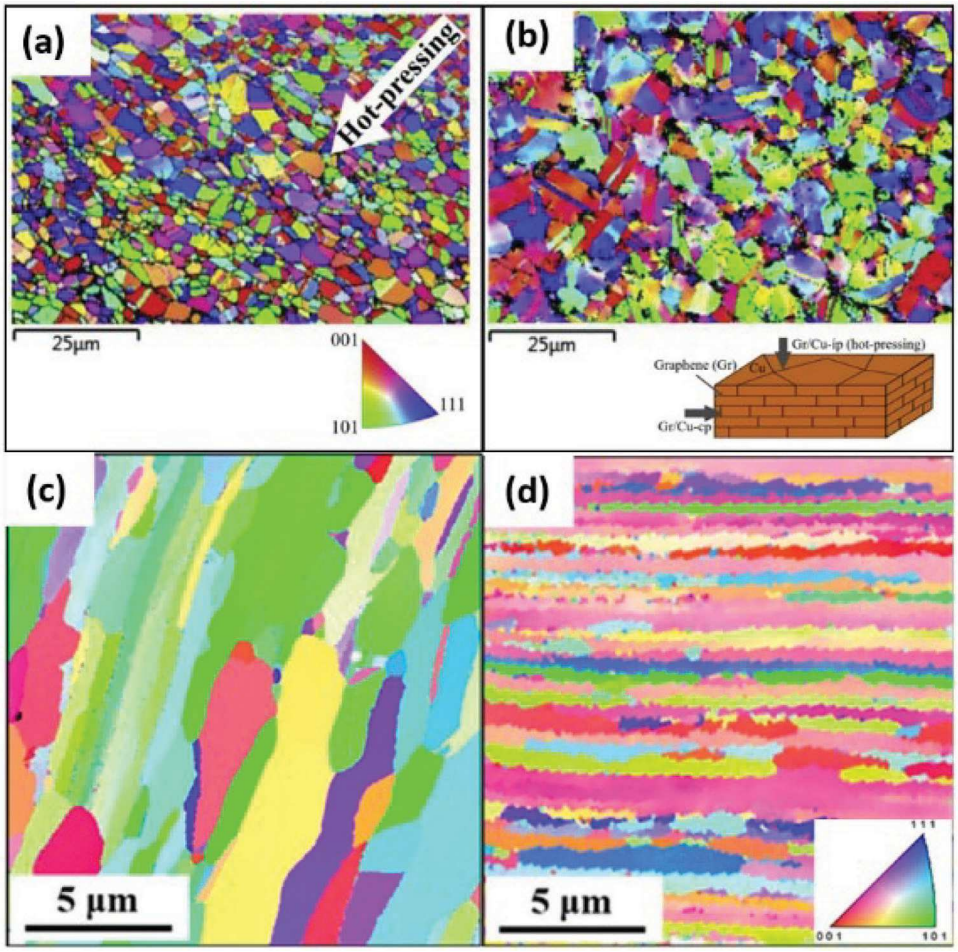


**Figure 9.** Microstructures of Cu and CGC after the consolidation process. a) Electron backscattered diffraction (EBSD) images of cross-plane (Gr/Cu-cp) and b) in-plane (Gr/Cu-ip) of the bulk CGC after hot pressing. The inset in (b) demonstrates the schematic of the "brick-and-mortar" microstructure of the CGC from flake powder metallurgy.[31] c) Electron backscattered diffraction (EBSD) inverse pole figures of annealed cold-drawn Cu wire and d) annealed cold-drawn CGC wire.[62] a,b) are reproduced (adapted) with permission.[31] Copyright 2019, Elsevier. c,d) are reproduced (adapted) with permission.[62] Copyright 2022, Elsevier.

conductivity. Therefore, in some studies, extrusion, drawing, or rolling[29,51,60–63,66,69,73] were further applied after hot pressing to achieve a better-condensed product. For example, in,[69] the electrical conductivity of the composite right after hot pressing was 52 MS $m^{-1}$ and then increased to 58.3 MS $m^{-1}$ after further hot extrusion.

The mechanical consolidation methods apply both shear and compressive stresses to CGCs. Shear stress can cause delamination of individual Gr layers in the direction of shear stress,[49] while the plastic elongation of a Cu matrix, in the normal direction of compressive stress, can break Gr structures into smaller flakes. Because the dispersion of Gr in a Cu matrix depends on loading conditions,[33] directional microstructural features in CGCs have been reported.[33,62]

As for cases after cold drawing and annealing, as shown in Figure 9c,d, the EBSD images along the drawing direction indicate more significant grain growth in Cu sample than in the CGC sample.[62] The differences in grain growth behavior might contribute to the Gr being dispersed along the grain boundaries, acting as the pining block for dislocation and preventing grain growth of the Cu matrix. Therefore, extrusion/drawing/rolling are usually applied in CGC synthesis to get a finer grain, thus improving mechanical strength (Hall-Petch effect). Luckily, since the electrical conductivity is not very sensitive to changes in grain size and dislocation density, the electrical performance of CGC conductors can be well preserved after extrusion/drawing/rolling with huge mechanical strengthening. For example, after severe plastic deformation, a pretty high tensile strength of 516 MPa (>200% of pure Cu) can be achieved with electrical conductivity at 95% IACS, which is still close to that of pure Cu.[62]

### *2.2.3. Other Attempts of Interface Engineering*

Another possible strategy to improve Cu-Gr interfacial strength is the use of bridging elements[53,63,65,66,68,73] or Cu sputtering.[37] In general, bridging elements decrease electrical conductivity because additional elements, despite their small fraction, act as defects and cause more pronounced electron scattering at the Cu—Gr interfaces. For example, tungsten particles (5–7 μm),[73]

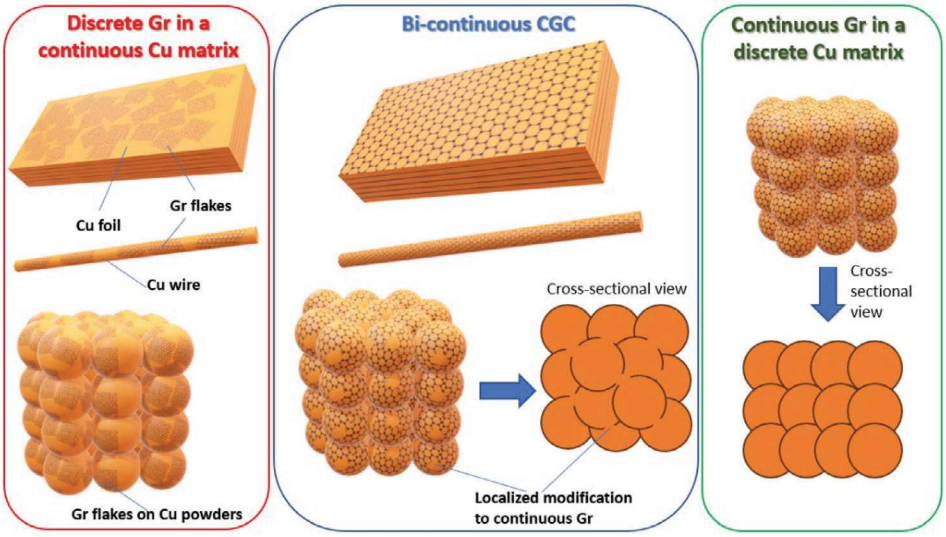


**Figure 10.** Common architectures of Cu—Gr network in CGCs: (Left to Right) discrete Gr in a continuous Cu matrix, bi-continuous CGC, and continuous Gr in a discrete Cu matrix. The orange color represents different Cu matrices, e.g., foil, wire, and powders. In the second and third columns, the cross-sectional views are shown to illustrate different internal Gr structures.

additional elements to the general synthesis of CGC, formed smaller tungsten carbide nanoparticles (15–20 nm) during high-energy ball milling and SPS. Indeed, the Cu—Gr interfacial bonding was improved but with lower electrical conductivity. A similar trend can be found in other studies using aluminum, lanthanum, and titanium[63,65,66] as bridging elements. Interestingly, an opposite trend has been also reported in one study.[53] Here, Ag and $CeO_2$ nanoparticles (20–50 nm) were formed on the surface of GO reinforcement through the hydrothermal reduction of $Ag^+$- and $Ce3^+$-rich solutions. The electrical conductivities of Ce-rGO/Cu and Ag-rGO/Cu composites were improved to 92.1% and 90% from 88.7% IACS for rGO/Cu composite, respectively. The authors attributed this enhancement to the good conductivity of Ag and the improved interface bonding for both Ce- and Ag-doped cases. The increased relative density and fewer agglomerations of rGO reinforcement caused by the bridging Ag or $CeO_2$ nanoparticles offset the drawbacks of increasing scattering centers for electron movements. Physical deposition of Cu was also used to improve the interfacial contact between Gr and Cu.[37] Here, a Cu substrate (50-μm-thick) was first coated with CVD-grown Gr and then an additional thin Cu film (thickness of ≈260 nm) was deposited onto the Gr layer. This sandwiched structure achieved 108.2% IACS. It is worth noting that Cu sputtering deposits a high-quality Cu layer while avoiding thermally induced residual stresses, but physical bombardment may damage Gr layers.

## 3. Summary of Recent Work on Synthesis and Performance of CGCs

This section summarizes the recent studies of CGCs, including different material processes, Gr sources, shape and size of Cu catalysts, microstructures of CGCs, and resultant performance. CGCs are commonly synthesized through a three-step fabrication (Gr synthesis, dispersion, and consolidation; see Figure 2) that results in three different architectures of types of Cu—Gr network, namely, discrete Gr in a continuous Cu matrix, bi-continuous CGC, and continuous Gr in a discrete Cu matrix (see **Figure 10**). For the first type, discrete Gr flakes produced by the top-down approaches (i.e., GO, rGO, and mechanical exfoliated Gr) are usually dispersed onto the surfaces of Cu foils, wires, or powders. For the second type, one obvious method is the bottom-up Gr synthesis (i.e., in situ and CVD Gr) on planarly or axially continuous Cu substrates, e.g., foils or wires, respectively. Note that achieving bi-continuous CGCs using Cu powders, both spheres, and flakes, requires an additional step, e.g., localized modification to Gr (see the bottom of the second column of Figure 10). This localized removal of Gr allows direct Cu—to—Cu contacts and, therefore, a continuous Cu network can be formed during consolidation. Without such modification, individual Cu powders (see the third column) are fully coated by Gr and, therefore, they remain discrete after consolidation.

**Table 2** summarizes CGCs with details on synthetic methods, a choice of materials, the performance of CGCs, composite size, architectures of Cu—Gr network, as well as scalability and economic efficiency of each CGC. For clarification, the scalability is mainly evaluated by the specifications of tools required by each CGC processing technique. For example, we assume that the size of CGCs processed by hot pressing or SPS will be constrained by a mold size (a few centimeters) in a sintering chamber. For economic efficiency, our evaluation is based on the current cost of raw materials, both Cu and Gr, from commercial vendors.

## 4. Electrical Properties of Copper-Graphene (Cu—Gr) Composites

Here we consider, based on a comprehensive literature review, how microstructures of CGCs and their electrical performances are correlated. To achieve this, we summarize normalized electrical conductivities of CGCs as a function of a Gr—to—Cu

**Table 2.** Processing route and performance of CGCs with scalability and economic efficiency evaluation.

| Copper source | Graphene type | Processing (Architecture of Cu-Gr network: G: continuous Gr; C: continuous Cu matrix; B: bi-continuous) | Sample size ([1]diameter for cylinder/wire; [2]thickness for plate/foil; [3]length × width × height for block) | Sample type (Cu: control sample of bare Cu) | Relative density [%] | Electrical conductivity [% IACS] | Ampacity [A $cm^{-2}$] | Scalability | Economic efficiency | References |
|---|---|---|---|---|---|---|---|---|---|---|
| $Cu(CH_3COO)_2$ | rGO | MLM + SPS | 30 mm[1] | Cu-2.5 vol%rGO-pH 6.6 | | 68.07 | | Medium | Good | [42] |
| | | (C) | | Cu-2.5 vol%rGO-pH 8.1 | | 64.09 | | | | |
| | | | | Cu-7.5 vol%rGO-pH 13.6 | | 65.79 | | | | |
| | | | | Cu-5 vol%rGO-pH 13.6 | | 69.12 | | | | |
| | | | | Cu-2.5 vol%rGO-pH 13.6 | | 65.67 | | | | |
| Cu power d<45 µm | rGO | Wet mixing + Cold pressing +Hot rolling | 3 mm[2] | Cu | 97 | 91.2 | | Medium | Medium | [51] |
| | | (C) | | Cu-0.25 wt.%rGO | 94.75 | 83.1 | | | | |
| | | | | Cu-0.50 wt.%rGO | 93.2 | 90.9 | | | | |
| | | | | Cu-0.75 wt.%rGO | 91.25 | 100 | | | | |
| | | | | Cu-1.00 wt.%rGO | 90 | 101.5 | | | | |
| Cu powder d = 63 µm | rGO | Wet mixing + Chemi-cal/thermal reduction + cold pressing | 10 mm[1] | Cu | | 100 | | Medium | Medium | [52] |
| | | | | Cu-0.28 wt.%rGO | | 8.7 | | | | |
| | | (C) | | Cu-1.1 wt.%rGO | | 12 | | | | |
| | | | | Cu-2.5 wt.%rGO | | 8.5 | | | | |
| Cu powder d = 5 µm | rGO | Ball milling + SPS | 15 mm[1] | Cu | 98 | 100.2 | | Medium | Medium | [53] |
| | | (C) | | Cu-Ce-0.25 wt.%rGO | 95.2 | 92.1 | | | | |
| | | | | Cu-Ag-0.25 wt.%rGO | 93.6 | 90 | | | | |
| | | | | Cu-0.25 wt.%rGO | 92.7 | 88.7 | | | | |
| Cu powder d = 20 µm | rGO | Ball mill + Stirring + Thermal reduction + SPS | 30 mm[1] | Cu | 98.9 | 95 | | Medium | Medium | [54] |
| | | (C) | | Cu-0.1 wt.%rGO | 98.5 | 91 | | | | |
| | | | | Cu-0.2 wt.%rGO | 98.4 | 87 | | | | |
| | | | | Cu-0.3 wt.%rGO | 98.1 | 80.2 | | | | |
| $Cu(CH_3COO)_2$ | rGO | MLM + SPS | 30 mm[1] | Cu | | 91 | | Medium | Good | [39] |

(*Continued*)

**Table 2.** (Continued)

| Copper source | Graphene type | Processing (Architecture of Cu-Gr network: G: continuous Gr; C: continuous Cu matrix; B: bi-continuous) | Sample size ([1]diameter for cylinder/wire; [2]thickness for plate/foil; [3]length × width × height for block) | Sample type (Cu: control sample of bare Cu) | Relative density [%] | Electrical conductivity [% IACS] | Ampacity [A $cm^{-2}$] | Scalability | Economic efficiency | References |
|---|---|---|---|---|---|---|---|---|---|---|
| | | (C) | | Cu-2.5 vol%small_rGO | | 82 | | | | |
| | | | | Cu-2.5 vol.%middle_rGO | | 74 | | | | |
| | | | | Cu-2.5 vol.%large_rGO | | 77 | | | | |
| $CuSO_4$ | rGO | Electrodeposition + Thermal reduction + SPS | 30 mm[1] | Cu | | 88.3 | | Medium | Good | [55] |
| | | (C) | | Cu-0.07 wt.%rGO | | 91.3 | | | | |
| | | | | Cu-0.10 wt.%rGO | | 85.7 | | | | |
| | | | | Cu-0.21 wt.%rGO | | 79.7 | | | | |
| Cu powder d = 10-15 µm | rGO | MLM + Stirring + Hot pressing | 24 mm[1] | Cu | 93 | 93 | | Medium | Poor | [56] |
| Cu powder d = 0.2-1 µm | | (C) | | Cu-10%_0.1 wt.%rGO/ submicron_Cu | 98 | 93 | | | | |
| | | | | Cu-50%_0.1 wt.%rGO/ submicron_Cu | 97 | 95 | | | | |
| | | | | Cu-10%_0.5 wt.%rGO/ submicron_Cu | 92 | 84 | | | | |
| | | | | Cu-30%_0.5 wt.%rGO/ submicron_Cu | 94 | 82 | | | | |
| | | | | Cu-50%_0.5 wt.%rGO/ submicron_Cu | 94 | 84 | | | | |
| $CuSO_4$ | rGO | Electrodeposition + Thermal reduction + SPS | 28 mm[1] | Cu | 98.59 | 96.91 | | Medium | Good | [57] |
| | | (C) | | Cu-0.013 wt.%rGO | 97.47 | 94.03 | | | | |
| | | | | Cu-0.024 wt.%rGO | 96.18 | 93.24 | | | | |
| | | | | Cu-0.034 wt.%rGO | 94.49 | 92.37 | | | | |
| $CuSO_4$ | Exfoliated Gr | Electrodeposition | 60 µm[2] | Cu-300 | | 86 | | Good | Good | [48] |
| | | (C) | | Cu-600 | | 90 | | | | |
| | | | | Cu-900 | | 93 | | | | |
| | | | | Cu-0.153 vol%Gr-300 | | 92 | | | | |
| | | | | Cu-0.156 vol%Gr-600 | | 94 | | | | |
| | | | | Cu-0.17 vol%Gr-900 (*300, 600 or 900 represents the corresponding electroplating current density in mA $cm^{-2}$*) | | 95 | | | | |

(*Continued*)

**Table 2.** (Continued)

| Copper source | Graphene type | Processing (Architecture of Cu-Gr network: G: continuous Gr; C: continuous Cu matrix; B: bi-continuous) | Sample size ([1]diameter for cylinder/wire; [2]thickness for plate/foil; [3]length × width × height for block) | Sample type (Cu: control sample of bare Cu) | Relative density [%] | Electrical conductivity [% IACS] | Ampacity [A $cm^{-2}$] | Scalability | Economic efficiency | References |
|---|---|---|---|---|---|---|---|---|---|---|
| Cu sheet t = 1 mm | Exfoliated Gr | Accumulative roll + Hot rolling (C) | 1 $mm^2$ | Cu | | 88–94.5 | | Good | Good | [49] |
| | | | | Cu-Gr | | 72.5-83 | | | | |
| Cu powder d<20 µm | In situ Gr | Ball milling + in situ growth of Gr + Hot pressing (G) | 30 $mm^1$ | Cu-2.5 vol%Gr | | 95 | | Medium | Medium | [31] |
| Cu powder d<5 µm | In situ Gr | In situ growth of Gr + Hot pressing + Hot rolling (B) | 30 $mm^1$ (sintered) | Cu | | 100.7 | | Medium | Medium | [29] |
| | | | 9 $mm^2$ (rolled) | Cu-0.387 vol%Gr | | 103.3 | | | | |
| Dendritic Cu powder d<50 µm | In situ Gr | In situ growth of Gr + (Ball milling) + SPS | 25 $mm^1$ | Cu | | 99.9 | | Medium | Medium | [59] |
| | | (without ball milling: G) | | Cu (ball-milled) | | 99.7 | | | | |
| | | (with ball milling: C) | | Cu-0.07 wt.%Gr | | 86.2 | | | | |
| | | | | Cu-0.070 wt.%Gr(ball-milled) | | 95.7 | | | | |
| Dendritic Cu powder d<50 µm | In situ Gr | In situ growth of Gr + Hot pressing + Cold rolling +Annealing | 20 $mm^1$ (sintered) 0.3 $mm^2$ (rolled) | Cu (sintered) | | 100.3 | | Medium | Medium | [60] |
| | | | | Cu (cold rolled) | | 98.4 | | | | |
| | | | | Cu (annealed) | | 100.1 | | | | |
| | | | | Cu-0.25 wt.%Gr (sintered) | | 98.2 | | | | |
| | | | | Cu-0.25 wt.%Gr (cold rolled) | | 93.7 | | | | |
| | | | | Cu-0.25 wt.%Gr (annealed) | | 96.1 | | | | |

(*Continued*)

**Table 2.** (Continued)

| Copper source | Graphene type | Processing (Architecture of Cu-Gr network: G: continuous Gr; C: continuous Cu matrix; B: bi-continuous) | Sample size ([1]diameter for cylinder/wire; [2]thickness for plate/foil; [3]length × width × height for block) | Sample type (Cu: control sample of bare Cu) | Relative density [%] | Electrical conductivity [% IACS] | Ampacity [A $cm^{-2}$] | Scalability | Economic efficiency | References |
|---|---|---|---|---|---|---|---|---|---|---|
| Flake Cu powder d = 30-50 µm, t = 0.6 µm | In situ Gr | In situ growth of Gr + SPS + Hot extrusion + Drawing (C) | 50 mm[1] (sintered) 3.5 mm[1] (extruded) 195 µm[1] (drawn) | Cu | | 83.6 | | Medium | Medium | [61] |
| | | | | Cu-0.3 vol%Gr | 97.2 | 79 | | | | |
| Cu powder d<20 µm, Cu powder d = 5–10 µm, Cu powder d = 5 µm | In situ Gr | In situ growth of Gr + Hot pressing + Cold forging + cold rolling + cold drawn + Annealing (C) | 20 mm[1] (sintered) 8 mm[1] (forged) 3.2 mm[1] (rolled) 0.49 mm[1] (drawn) | Cu (sintered) | | 99.2 | | Medium | Medium | [62] |
| | | | | Cu (drawn) | | 95.65 | | | | |
| | | | | Cu (annealed) | | 99.01 | | | | |
| | | | | Cu-0.0218 wt.%Gr (sintered) | | 98.05 | | | | |
| | | | | Cu-0.0218 wt.%Gr (drawn) | | 94.85 | | | | |
| | | | | Cu-0.0218 wt.%Gr (annealed) | | 97.28 | | | | |
| | | | | Cu-0.03 wt.%Gr (sintered) | | 97.85 | | | | |
| | | | | Cu-0.03 wt.%Gr (drawn) | | 93.2 | | | | |
| | | | | Cu-0.03 wt.%Gr (annealed) | | 97.41 | | | | |
| Cu powder d<20 µm | In situ Gr | In situ growth of Gr + Hot pressing + Cold rolling + Annealing (C) | 30 mm[1] (sintered) 0.3 mm[2] (rolled) | Cu-0.0027 wt.%Gr-$Al_2O_3$ | | 96.95 | | Medium | Medium | [63] |
| | | | | Cu-0.0096 wt.%Gr-$Al_2O_3$ | | 94.1 | | | | |
| | | | | Cu-0.032 wt.%Gr-$Al_2O_3$ | | 89.08 | | | | |
| Cu powder d = 35-38 µm | In situ Gr | Ball milling + in situ growth of Gr + SPS | 40 mm[1] | Cu | 99 | 98 | | Medium | Medium | [64] |

(*Continued*)

**Table 2.** (Continued)

| Copper source | Graphene type | Processing (Architecture of Cu-Gr network: G: continuous Gr; C: continuous Cu matrix; B: bi-continuous) | Sample size ([1]diameter for cylinder/wire; [2]thickness for plate/foil; [3]length × width × height for block) | Sample type (Cu: control sample of bare Cu) | Relative density [%] | Electrical conductivity [% IACS] | Ampacity [A $cm^{-2}$] | Scalability | Economic efficiency | References |
|---|---|---|---|---|---|---|---|---|---|---|
| | (C) | | Cu-0.35 wt.%Gr | 99.2 | 91 | | | | | |
| | | | | Cu-0.70 wt.%Gr | 99.3 | 86 | | | | |
| | | | | Cu-1.05 wt.%Gr | 99.4 | 77 | | | | |
| Cu powder d ≈ 20 µm | In situ Gr | In situ growth of Gr + Hot pressing + Cold forging + Cold rolling + Cold drawing + Annealing (C) | 12.4 mm[1] (sintered) 8 mm[1] (forged) 3 mm[1] (rolled) 0.49 mm[1] (drawn) | Cu | | 99.17 | | Medium | Medium | [65] |
| | | | | Cu-0.03 wt.%Gr-La2O3 (sintered at 900 °C) | | 99 | | | | |
| | | | | Cu-0.04 wt.%Gr-$La_2O_3$ (sintered at 900 °C) | | 96 | | | | |
| | | | | Cu-0.06 wt.%Gr-$La_2O_3$ (sintered at 900 °C) | | 92.7 | | | | |
| | | | | Cu-0.095 wt.%Gr-$La_2O_3$ (sintered at 900 °C) | | 87 | | | | |
| | | | | Cu-0.18 wt.%Gr-$La_2O_3$ (sintered at 900 °C) | | 78.5 | | | | |
| | | | | Cu-0.044 wt.%Gr-$La_2O_3$ (sintered at 700 °C) | | 91.4 | | | | |
| | | | | Cu-0.41 wt.%Gr-$La_2O_3$ (sintered at 800 °C) | | 93.8 | | | | |
| | | | | Cu-0.044 wt.%Gr-$La_2O_3$ (sintered at 900 °C) | | 96.1 | | | | |
| | | | | Cu-0.042 wt.%Gr-$La_2O_3$ (sintered at 1000 °C) | | 97.5 | | | | |
| | | | | Cu-Gr-$La_2O_3$ (drawn and annealed) | | 99.5 | | | | |
| Cu powder d<20 µm | In situ Gr | In situ growth of Gr + Hot pressing + Cold forging + Cold rolling + Cold drawn + Annealing (C) | 12.4 mm[1] (sintered) 8 mm[1] (forged) 3.2 mm[1] (rolled) 0.49 mm[1] (drawn) | Cu | | 99.17 | | Medium | Medium | [66] |
| | | | | Cu-0.1266 wt.%Gr-Al | | 92.1 | | | | |
| | | | | Cu-0.073 wt.%Gr-Mg | | 81.55 | | | | |
| | | | | Cu-0.1509 wt.%Gr-Zn | | 81.68 | | | | |
| | | | | Cu-0.1602 wt.%Gr-Ca | | 83.92 | | | | |
| | | | | Cu-0.052 wt.%Gr-Ti | | 95.2 | | | | |
| Cu powder d<76 µm | CVD CNTs | Cu-Cr Alloying/Co-deposition + CVD growth of CNTs + SPS | 30 mm[1] | Cu | 97 | 100 | | Medium | Medium | [68] |

(*Continued*)

**Table 2.** (Continued)

| Copper source | Graphene type | Processing (Architecture of Cu-Gr network: G: continuous Gr; C: continuous Cu matrix; B: bi-continuous) | Sample size ([1]diameter for cylinder/wire; [2]thickness for plate/foil; [3]length × width × height for block) | Sample type (Cu: control sample of bare Cu) | Relative density [%] | Electrical conductivity [% IACS] | Ampacity [A $cm^{-2}$] | Scalability | Economic efficiency | References |
|---|---|---|---|---|---|---|---|---|---|---|
| | | Cu-0.5 vol%CNT-Cr-1 (co-deposited) (C) | 95 | 83<br>Cu-0.5 vol%CNT-Cr(alloy) | 96 | 92.9 | | | | |
| Cu foil t ≈ 9–45 µm | CVD Gr | CVD growth of Gr + hot pressing (B) | ≈150 $µm^2$ | Cu (pristine)<br>Cu (Gr removed)<br>Cu-0.003 vol%Gr<br>Cu-0.008 vol%Gr | | 97<br>112.5<br>116.3<br>117.4 | | Medium | Medium | [32] |
| Cu wire d = 1 mm | CVD Gr | CVD growth of Gr + Hot extrusion + Cold drawn (As CVD grown: B) (As extruded: C) (As drawn: C) | 5 mm[1] (extruded) 1 mm[1] (drawn) | Cu (unprocessed)<br>Cu (extruded)<br>Cu (drawn)<br>Annealed-Cu (unprocessed)<br>Annealed-Cu (extruded)<br>Annealed-Cu (drawn)<br>Cu-0.00055 vol%Gr (As CVD grown)<br>Cu-0.00025 vol%Gr (extruded)<br>Cu-0.00025 vol%Gr (drawn) | | 96.7<br>94.9<br>85.5<br>88.8<br>87.4<br>86.7<br>101<br>95.7<br>94 | | Good | Good | [33] |
| Cu powder d = 20 µm | CVD Gr | CVD growth of Gr + Hot pressing + Hot extrusion + Cold drawn (B) | 20 mm[1] (sintered) 5 mm[1] (extruded) 1 mm[1] (drawn) | Cu (sintered)<br>Cu (extruded)<br>Cu (drawn)<br>Cu-0.085 vol%Gr (sintered)<br>Cu-0.085 vol%Gr (extruded)<br>Cu-0.085 vol.%Gr (drawn) | | 99.3<br>95.5<br>97.4<br>89.5<br>100.3<br>99.7 | | Medium | Medium | [69] |
| Cu powder d≈20 µm | CVD Gr | CVD growth of Gr + Hot pressing | 20 mm[1] | Cu | 98.3 | 100.1 | | Medium | Medium | [70] |

(*Continued*)

**Table 2.** (Continued)

| Copper source | Graphene type | Processing (Architecture of Cu-Gr network: G: continuous Gr; C: continuous Cu matrix; B: bi-continuous) | Sample size ([1]diameter for cylinder/wire; [2]thickness for plate/foil; [3]length × width × height for block) | Sample type (Cu: control sample of bare Cu) | Relative density [%] | Electrical conductivity [% IACS] | Ampacity [A $cm^{-2}$] | Scalability | Economic efficiency | References |
|---|---|---|---|---|---|---|---|---|---|---|
| | (G) | | Cu-0.068 vol.%Gr | 98.2 | 99.3 | | | | | |
| | | | | Cu-0.076 vol.%Gr | 98.2 | 99.3 | | | | |
| | | | | Cu-0.116 vol.%Gr | 98.1 | 99.2 | | | | |
| | | | | Cu-0.141 vol.%Gr | 98.0 | 99.1 | | | | |
| Cu foil t = 50 µm | CVD Gr | CVD growth of Gr + Cu sputtering | 45 µm[2] | Annealed Cu | | 98.5 | | Medium | Poor | [37] |
| | | (B) | | Gu-0.0008 vol%Gr | | 100.2 | | | | |
| | | | | Cu-0.0008 vol%Gr-Cu | | 108.2 | | | | |
| Cu wire d = 10, 25, 80 µm | CVD Gr | CVD growth of Gr | 10/25/80 µm[1] | Cu (10 µm) | | 90.1 | | Medium | Medium | [34] |
| | | (B) | | Cu (25 µm) | | 86 | | | | |
| | | | | Cu (80 µm) | | 100 | | | | |
| | | | | Annealed Cu (10 µm) | | 72.9 | 2.43 | | | |
| | | | | Annealed Cu (25 µm) | | 84 | 1.77 | | | |
| | | | | Annealed Cu (80 µm) | | 101 | 0.77 | | | |
| | | | | Cu-Gr Axial wire (10 µm) | | 123.8 | 4.26 | | | |
| | | | | Cu-Gr Axial wire (25 µm) | | 107.6 | 2.15 | | | |
| | | | | Cu-Gr Axial wire (80 µm) | | 105.9 | 0.8 | | | |
| PVD Cu nano wire | CVD Gr | PVD and E-beam lithography + CVD growth of Gr | 60 nm × 180 nm × 10/20 µm[3] | Cu (Gr removed) (180 nm) | | 32 | 65.1 | poor | poor | [71] |
| | | | 60 nm × 280nm × 10/20 µm[3] | Cu (Gr removed) (280 nm) | | 34 | 57.4 | | | |
| | | (B) | | Cu -Gr (180 nm) | | 36 | 77.3 | | | |
| | | | | Cu -Gr (280 nm) | | 39 | 63.6 | | | |
| Cu wire d = 200 µm | CVD Gr | CVD growth of Gr + Twisting + Annealing + Drawing + Repeating the processes | 30 µm[1] | Cu-0 | 98.0 | 97.1 | | Good | Good | [72] |

(*Continued*)

**Table 2.** (Continued)

| Copper source | Graphene type | Processing (Architecture of Cu-Gr network: G: continuous Gr; C: continuous Cu matrix; B: bi-continuous) | Sample size ([1]diameter for cylinder/wire; [2]thickness for plate/foil; [3]length × width × height for block) | Sample type (Cu: control sample of bare Cu) | Relative density [%] | Electrical conductivity [% IACS] | Ampacity [A $cm^{-2}$] | Scalability | Economic efficiency | References |
|---|---|---|---|---|---|---|---|---|---|---|
| | | Cu-1 | 97.7 | 95.9 | | | | | | |
| | | (As CVD grown: B) | | Cu-2 | 97.7 | 93.6 | | | | |
| | | (After twisting: C) | | Cu-3 | 97.7 | 93.3 | | | | |
| | | | | Cu-4 | 97.7 | 91.4 | | | | |
| | | | | Cu-5 | 97.7 | 91.6 | | | | |
| | | | | Cu-6 | 97.9 | 91.6 | | | | |
| | | | | Cu-Gr-0 | 98.0 | 96.7 | 2 | | | |
| | | | | Cu-Gr-1 | 97.6 | 95.2 | 2.2 | | | |
| | | | | Cu-Gr-2 | 97.6 | 93.1 | 2.1 | | | |
| | | | | Cu-Gr-3 | 97.6 | 88.0 | 2.2 | | | |
| | | | | Cu-Gr-4 | 97.7 | 88.1 | 4.1 | | | |
| | | | | Cu-Gr-5 | 97.8 | 87.8 | 4.8 | | | |
| | | | | Cu-Gr-6 | 98.0 | 86.2 | 6 | | | |
| | | | | (* 0–6 represents cycles of processing*) | | | | | | |
| Cu powder d<44 µm | In situ Gr | Ball milling + in situ growth of Gr + Plasma assisted milling (PAM) + Hot pressing + Hot rolling | 30 mm[1] (sintered) 1.5 $mm^2$ (rolled) | Cu | | 90.6 | | Medium | Medium | [73] |
| | | | | Cu-Gr (without PAM) | | 71.3 | | | | |
| | | | | Cu-Gr (with PAM) | | 75.5 | | | | |
| Cu powder d<75 µm | GO | Ball milling + Hot pressing (600 °C or 700 °C) | 25.4 mm[1] | Cu (600 °C) | 83.5 | 77 | | Medium | Medium | [40] |

(*Continued*)

**Table 2.** (Continued)

| Copper source | Graphene type | Processing (Architecture of Cu-Gr network: G: continuous Gr; C: continuous Cu matrix; B: bi-continuous) | Sample size ([1]diameter for cylinder/wire; [2]thickness for plate/foil; [3]length × width × height for block) | Sample type (Cu: control sample of bare Cu) | Relative density [%] | Electrical conductivity [% IACS] | Ampacity [A $cm^{-2}$] | Scalability | Economic efficiency | References |
|---|---|---|---|---|---|---|---|---|---|---|
| | | (C) | | Cu (700 °C) | 88.4 | 99 | | | | |
| | | | | Cu-1 wt.% GO (600 °C) | 92.6 | 94 | | | | |
| | | | | Cu-1 wt.%GO (700 °C) | 91.6 | 81 | | | | |
| Cu plate t = 4 mm | Gr (purchased) | Hole drilling + Gr filling + Friction stirring (C) | 100 mm × 40 mm × 4 mm[3] | Cu | | 98.5 | | Good | Good | [77] |
| | | | | Cu-8 vol%Gr-50 | | 97.4 | | | | |
| | | | | Cu-8 vol%Gr-100 | | 97.3 | | | | |
| | | | | Cu-8 vol%Gr-150 | | 97.15 | | | | |
| | | | | Cu-8 vol%Gr-200 (*50–200 represents the traverse speed of friction stirring in mm $min^{-1}$*) | | 97.4 | | | | |
| Cu powder d = 6–50 µm | Gr (purchased) | Magnetic stirring + Ultrasonicate (or conventional) pressureless sintering (C) | 10 mm[1] | Cu (ultrasonicated) | 88.8 | 82.6 | | Good | Medium | [41] |
| | | | | Cu (conventional) | 78.1 | 74.51 | | | | |
| | | | | Cu-0.25 wt.%Gr (ultrasonicated) | 87.2 | 84.26 | | | | |
| | | | | Cu-0.5 wt.%Gr (ultrasonicated) | 86.0 | 86.4 | | | | |
| | | | | Cu-1 wt.%Gr (ultrasonicated) | 84.8 | 88.3 | | | | |
| | | | | Cu-1.5 wt.%Gr(ultrasonicated) | 83.8 | 84.4 | | | | |
| | | | | Cu-0.25 wt.%Gr (conventional) | 76.9 | 75.34 | | | | |
| | | | | Cu-0.5 wt.%Gr (conventional) | 76.2 | 76.61 | | | | |
| | | | | Cu-1 wt.%Gr (conventional) | 75.6 | 78.12 | | | | |
| | | | | Cu-1.5 wt.%Gr(conventional) | 75.4 | 75.64 | | | | |
| Cu foil | Gr (purchased) | Hot extrusion (C) | 2 mm[1] | Cu | | 100.89 | | Good | Poor | [36] |
| | | | | Cu-5ppmGr (low defects) | | 102.75 | | | | |
| | | | | Cu-10 ppmGr (low defects) | | 103.1 | | | | |
| | | | | Cu-15 ppmGr (low defects) | | 103.61 | | | | |
| | | | | Cu-15 ppmGr (high defects) | | 101.2 | | | | |
| | | | | Cu-35 ppmGr (high defects) | | 102.07 | | | | |
| | | | | Cu-100 ppmGr (high defects) | | 102.75 | | | | |
| | | | | Cu-250 ppmGr (high defects) | | 102.41 | | | | |

(*Continued*)

**Table 2.** (Continued)

| Copper source | Graphene type | Processing (Architecture of Cu-Gr network: G: continuous Gr; C: continuous Cu matrix; B: bi-continuous) | Sample size ([1]diameter for cylinder/wire; [2]thickness for plate/foil; [3]length × width × height for block) | Sample type (Cu: control sample of bare Cu) | Relative density [%] | Electrical conductivity [% IACS] | Ampacity [A $cm^{-2}$] | Scalability | Economic efficiency | References |
|---|---|---|---|---|---|---|---|---|---|---|
| $CuSO_4$ | CVD Gr | CVD growth of Gr + Gr Fiber extraction + Cu electroplating (B) | <50 µm[1] | Cu(shell)-Gr(core) wire | | 63.7 | 1 | Good | Good | [79] |
| $CuSO_4$ | rGO | rGO Fiber mesh synthesis + electroplating (C) | A few cm × a few cm mesh | Cu(shell)-rGO(core)-mesh-1 | | 3.1 | | Good | Good | [80] |
| | | | | Cu(shell)-rGO(core)-mesh-2 | | 5.2 | | | | |
| | | | | Cu(shell)-rGO(core)-mesh-3 | | 9.1 | | | | |
| | | | | Cu(shell)-rGO(core)-mesh-4 | | 15.8 | | | | |
| | | | | Cu(shell)-rGO(core)-mesh-5 (*1–5 represents the electroplating voltage in V*) | | 55.1 | | | | |
| $CuSO_4$ | CNT + CVD Gr | Electroplating on carbon nanotube fiber (CNTF) + CVD growth of Gr (B) | ≈20 µm[1] | Cu | | | 0.14 | Good | Good | [81] |
| | | | | CNTF-Cu | | | 0.13 | | | |
| | | | | Annealed CNTF-Cu | | | 0.15 | | | |
| | | | | CNTF-Cu-Gr | | | 0.17 (in vacuum) | | | |
| Cu sputtering | GO + Graphite | GO film synthesis + Annealing reduction + Rolling + Cu sputtering (C) | 8.8 µm[2] | Cu-LargeGr-film (Cu side) | | 10.1 | | Good | Poor | [82] |
| | | | | Cu-LargeGr-film (Gr side) | | 9.76 | | | | |
| Cu(111) foil t = 25 µm | CVD Gr | CVD growth of Gr + Oxidation in air + Hot pressing/SPS (B) | | Cu-Gr (SPS) | | 108.6 | | Medium | Medium | [35] |
| | | | | Cu-Gr (hot pressed) | | 98.8 | | | | |

(*Continued*)

**Table 2.** (Continued)

| Copper source | Graphene type | Processing (Architecture of Cu-Gr network: G: continuous Gr; C: continuous Cu matrix; B: bi-continuous) | Sample size ([1]diameter for cylinder/wire; [2]thickness for plate/foil; [3]length × width × height for block) | Sample type (Cu: control sample of bare Cu) | Relative density [%] | Electrical conductivity [% IACS] | Ampacity [A $cm^{-2}$] | Scalability | Economic efficiency | References |
|---|---|---|---|---|---|---|---|---|---|---|
| Dendritic Cu powder d = 3 µm | Gr (purchased) or rGO | Mechanical stirring + Thermal reduction + SPS | 20 mm[1] | Cu | | 99.1 | | Medium | Medium | [85] |
| | | (C) | | Cu-0.3 wt.%Gr | | 84.2 | | | | |
| | | | | Cu-0.3 wt.%rGO | | 73.4 | | | | |
| Cu powder d = 44 µm | In situ Gr | Ball milling + in situ growth of Gr + Hot pressing | 9 mm[1] | Cu | | 97.8 | | Medium | Medium | [38] |
| | | | | Cu-1.6 vol%Gr | | 97.1 | | | | |
| | | (G) | | Cu-2.5 vol%Gr | | 93.8 | | | | |
| $Cu_{33}Mn_{67}$ | CVD/in situ Gr | Chemical etching + CVD + Pyrolysis + Cold rolling + Annealing | 0.2 mm[2] | Cu | 93.7 | 83.5 | | Poor | Poor | [86] |
| | | | | Cu-Gr (800 °C) | 91.9 | 98 | | | | |
| | | (B) | | Cu-Gr (850 °C) | 91.4 | 87 | | | | |
| Cu wire d = 10,25,80 µm | CVD Gr | CVD growth of Gr + Ni sputtering | 10/25/80 µm[1] | Cu-Gr-Ni Axial wire (10 µm) | | 105 | 0.315 | Medium | Poor | [102] |
| | | (B) | | Cu-Gr-Ni Axial wire (25 µm) | | 91.8 | 0.185 | | | |
| | | | | Cu-Gr-Ni Axial wire (80 µm) | | 95.6 | 0.108 | | | |

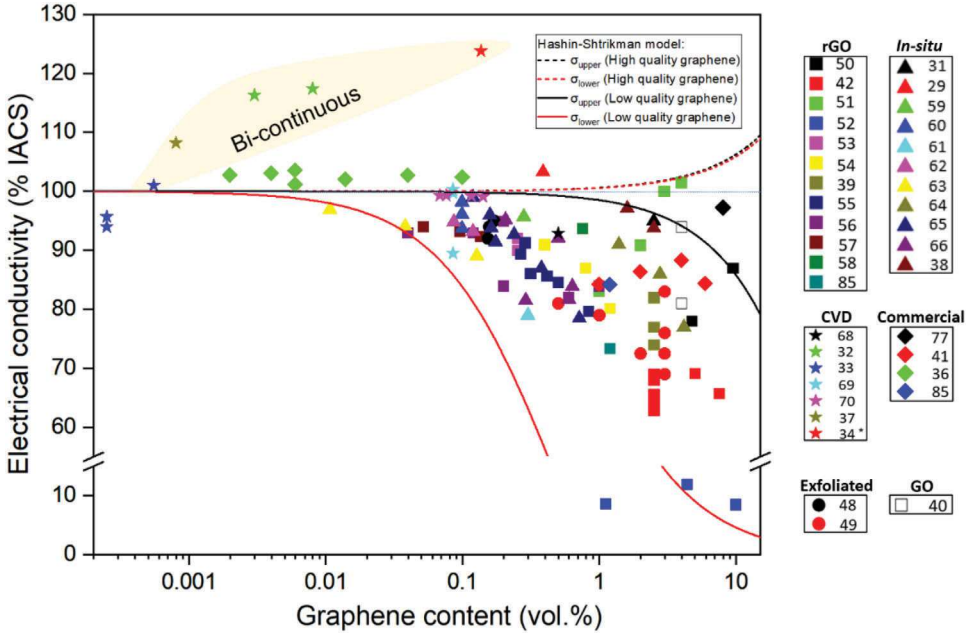


**Figure 11.** Electrical conductivity versus carbon volume fraction of composites published in recent years. *The Gr volume fraction of,[34] indicated by ★, is estimated by calculating 10 layers of Gr wrapping the axially continuous Gr Cu wire. The upper and lower boundaries for CGCs reinforced with high-quality Gr (CVD Gr) and low-quality Gr (rGO, GO, in situ growth, and mechanical exfoliated Gr) are calculated by Equations (1) and (2), respectively.

volume fraction, as shown in **Figure 11**. To interpret different trends in the figure, we utilize a model for a two-phase mixture, i.e., the Hashin–Shtrikman model,[103] which has also been adopted by others.[50,56] The upper and lower boundaries ( $\sigma_U$ and $\sigma_L$, respectively) for the electrical conductivity of the Cu-Gr composite system are given as below:

$$\sigma_{\mathrm{U}} = \sigma_{\mathrm{Cu}} + \frac{V_{\mathrm{Gr}}}{\frac{1}{\sigma_{\mathrm{Gr}}-\sigma_{\mathrm{Cu}}} + \frac{V_{\mathrm{Cu}}}{3\sigma_{\mathrm{Cu}}}} \quad (1)$$

$$\sigma_{\mathrm{L}} = \sigma_{\mathrm{Gr}} + \frac{V_{\mathrm{Cu}}}{\frac{1}{\sigma_{\mathrm{Cu}}-\sigma_{\mathrm{Gr}}} + \frac{V_{\mathrm{Gr}}}{3\sigma_{\mathrm{Gr}}}} \quad (2)$$

where $\sigma_{\mathrm{Cu}}$ and $\sigma_{\mathrm{Gr}}$ are the electrical conductivity of Cu and Gr and $V_{\mathrm{Cu}}$ and $V_{\mathrm{Gr}}$ are the volume fractions of Cu and Gr, respectively. For this analysis, we assume that $\sigma_{\mathrm{Cu}} = 5.81$ MS m$^{-1}$[13] for all cases, while two different values of $\sigma_{\mathrm{Gr}}$ are used to capture the effect of Gr quality on the overall conductivity of the Cu-Gr composites. As to specifics, $\sigma_{\mathrm{Gr}} = 0.1$ MS m$^{-1}$[28] for Gr with low conductivity (e.g., in situ growth, rGO, and mass-produced mechanically exfoliated flakes) and $\sigma_{Gr} = 100$ MS m$^{-1}$[12] for Gr with high conductivity (e.g., CVD growth).

Our results show two very distinctive trends depending on the types of Gr in CGCs: 1) the solid red/black curves, below 100% IACS, for low-quality Gr and 2) the red/black dashed curves, above 100% IACS, for high-quality Gr. For CGCs with <100% IACS, their conductivities fall between the predicted $\sigma_{\mathrm{L}}$ and $\sigma_{\mathrm{U}}$ values by the Hashin-Shtrikman model. This is an expected conclusion because $\sigma_{\mathrm{Gr}} = 0.1$ MS m$^{-1}$ is lower than $\sigma_{Cu}$ and, therefore, a higher Gr—to—Cu volume fraction results in a lower Cu—Gr conductivity. The low $\sigma_{Gr}$ can be attributed to excessive Gr layers/agglomeration, chemical residues in Gr, and discrete Gr structures. Obviously, the opposite trend is predicted for $\sigma_{\mathrm{Gr}} = 100$ MS m$^{-1}$, e.g., the electrical conductivity of CGCs increases with increasing volume fraction. Therefore, a low- and high- volume fraction of graphene reinforcement is suggested when reinforcing low- and high-quality graphene into copper matrix, respectively. However, there is a considerable discrepancy between the prediction by the model[32,71] and experimental data (see the red/black dashed curves and *Bi-continuous network* in Figure 11. In the following, several studies are reviewed to offer feasible explanations for this discrepancy.

First, Mehta et al.[71] reported a nanoscale Cu wires (diameter ≈250 nm) coated by Gr synthesized by plasma enhanced CVD (PECVD) at 650 °C. To confirm the Gr enhanced conductivity, Gr was removed by oxygen plasma (Cu—NG), which resulted in about a 12% decrease in electrical conductivity. The authors argued that electron scattering becomes partially elastic when the free surfaces of Cu are coated by high-quality Gr, as schematically shown in **Figure 12a**. They pointed out two mechanisms, the low density of states in Gr and the weak electronic coupling between Gr and Cu surfaces (see the DFT calculation in Figure 12b).[71] Kashani et al. performed CVD Gr growth at ≈1000 °C on microscale Cu wires with 10, 25, and 80-µm diameters and showed 41%, 22%, and 4.2% reduction, respectively, in their resistivity compared to their pure Cu wire counterparts,[34] Figure 12c. The authors explained these size-dependent electrical properties by a larger surface-to-volume ratio with a decrease in wire diameter and, as a result, a more pronounced effect directly from Gr. Considering the size dependency, smaller size of a copper substrate is preferred to achieve higher electrical enhancement from graphene coating. Note that directly comparing the Gr -enhanced

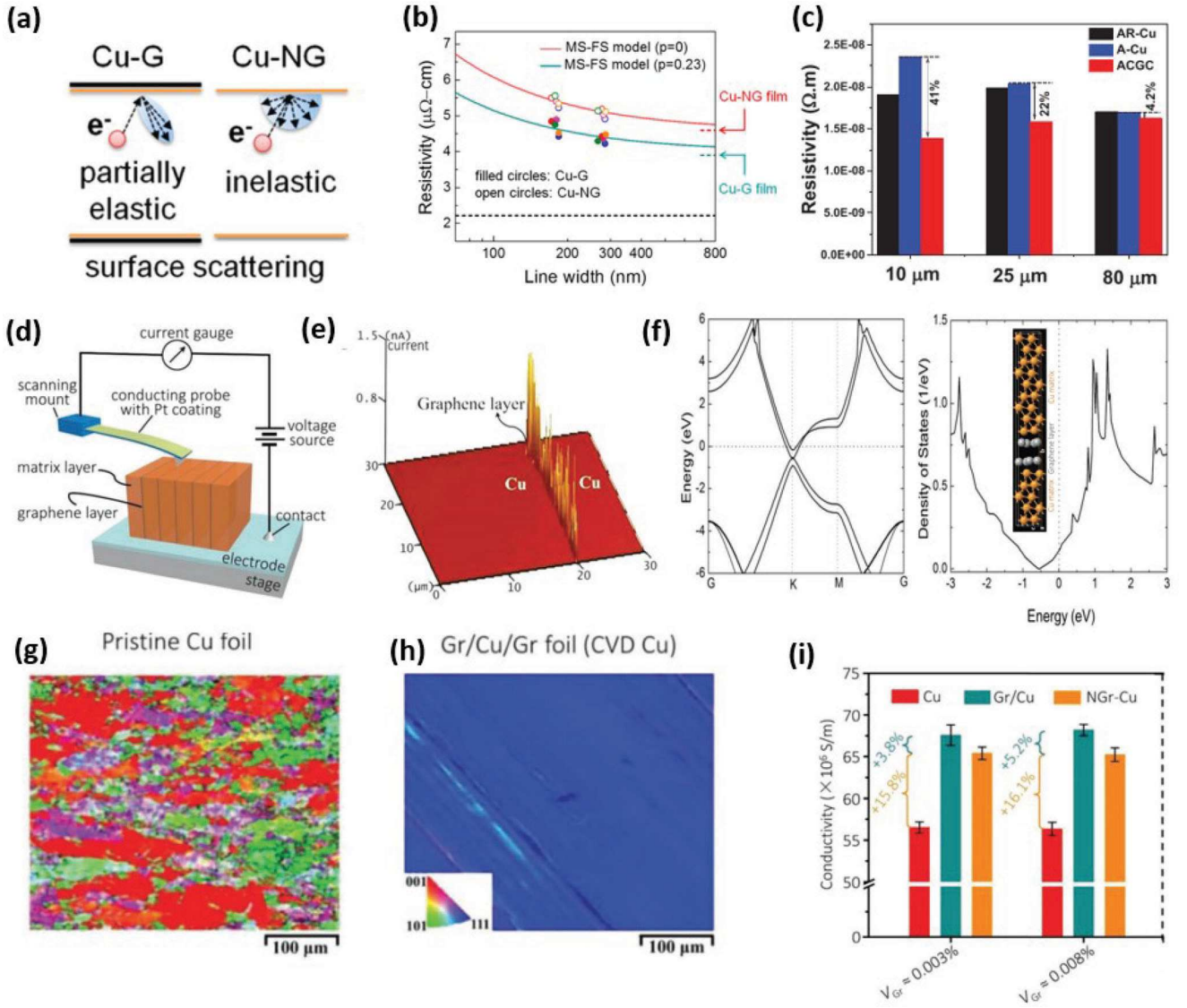


**Figure 12.** Mechanisms for the enhanced electrical conductivity of CGCs. a) Schematic illustrating partial elastic and complete inelastic surface scattering of incident electrons along the current direction. b) Measured resistivity values of Cu nanowires (CuNWs) with (filled circles) and without Gr (open circles) coating, as a function of NW width.[71] c) Size-dependent electrical resistivity of the as-received (AR—Cu), annealed (A—Cu), and axially continuous Gr—Cu (ACGC) wires with different wire diameters (i.e., $d_w$ = 10, 25, and 80 μm).[34] d) Schematic of current mapping of sandwich-structured CGC via peak force tunneling atomic force microscope (PF-AFM). e) Current mapping image of a 30 μm × 30 μm Cu/Gr/Cu interface area; the peak current along the Gr layer is three orders of magnitude higher than that in the surrounding pure Cu matrix. f) Electronic band structure and density of state of Gr embedded in Cu layers, calculated by VASP. The inset in the plot of the density of the state is the model system of this Cu/Gr/Cu composite in VASP.[32] g,h) EBSD images of the Cu foil substrates before and after CVD Gr growth, respectively. i) Electrical conductivities of pure Cu, Gr/Cu, and NGr-Cu (CVD Gr on Cu foil was etched away by oxygen plasma) samples.[32] a,b) reprinted (adapted) with permission from.[71] Copyright 2015 American Chemical Society. (c) is reproduced with permission.[34] Copyright 2021, John Wiley and Sons. (d), (e), (f), (g), (h), and (i) are reproduced (adapted) with permission.[32] Copyright 2019, John Wiley and Sons.

conductivity from[34] and[71] is still difficult because they used different catalysts and CVD conditions and subsequently different Gr quality, e.g., they reported different Raman measurements in their work.

Other feasible mechanisms are proposed by Cao et al.[32] The authors argued that the continuous planar Gr structures, when embedded between Cu foils, can be doped by the electrons of Cu. Such electron-doped Gr, combined with extremely high electron mobility, can form highly conductive continuous paths for electrons in the CGC. For experimental validation, a few Cu foils, individually coated with CVD-grown monolayer Gr, were stacked together and then processed by hot pressing consolidation. Then, the authors mapped the localized current at a different location on the cross-section of the sandwich Cu—Cr—Cu structure via the peak force tunneling atomic force microscope (PF-AFM, see Figure 12d). The results in Figure 12e show a current spike near Gr compared to the neighboring Cu layers, indicating much higher local conductivity near the embedded

Gr. Furthermore, their computational model, based on density functional theory, predicted that a Cu/bilayer-Gr/Cu composite exhibits the electron-doped Gr structures (doping density ≈5.5 × $10^{21}$ $cm^{-3}$) with nonzero density of states near Fermi energy (see Figure 12f). In addition, unusual recrystallization and grain coarsening during CVD Gr growth can also contribute to the enhanced electrical conductivity of CGCs. For example, EBSD images in Figure 12g,h show that the microstructures of a thin Cu foil catalyst transition from polycrystalline to single crystalline. Note that Cu(111) is the preferred crystal orientation after a CVD process to minimize the lattice mismatch between Cu and Gr. Furthermore, the electrical conductivities of three different samples, Cu foil (red columns), CGC (aqua columns), and the CGC after etching away the Gr (orange columns), were characterized, as summarized in Figure 12i, to quantify the contributions from Gr and microstructural changes in Cu. The results indicate that a 4–5% improvement is from Gr while about a 16% improvement is associated with the CVD-process-dependent microstructural changes in Cu.

In summary, our review strongly suggests that the spatial distribution and directional continuity of both a Gr network and a Cu matrix play an important role in the electrical conductivity of CGCs. Cu—Gr interfacial contacts in CGC are intrinsically weak without any chemical Cu—Gr bonds and the Cu-Gr contact resistance is relatively high compared to the resistance of both Cu and Gr. CGCs consisting of smaller particles/flakes of either Gr or Cu likely suffer from lower conductivity due to interfacial electron scattering at Cu—Gr junctions. On the other hand, it seems CGCs with bi-continuous microstructures (see Figure 10), aligned in the electrical flow, achieve better electrical conductivity. For example, a bundle of Gr -coated 1-mm-diameter Cu wires[33] was mechanically extruded together. This mechanical process damaged the continuous Gr network and resulted in a decrease in the electrical conductivity from 101% IACS to 95.7%. The continuity of a Cu network is also important for CGC performance, e.g., demonstrated by CGC based on in situ Gr growth on Cu powders.[59] In this work, Cu powders were separated by Gr structures, even after consolidation, and the CGC achieved 86.2% IACS. When Gr -coated Cu powders were partially damaged by ball milling, the conductivity of the modified CGC became 95.7% IACS. The author explained this improvement was based on direct Cu-to-Cu contacts within the modified CGC. Finally, it is important to emphasize that all the CGCs with >103% IACS in Figure 11 have the bi-continuous Cu—Gr network.[32–34,37] Finally, the relatively low conductivity of the CGCs prepared by powder metallurgy, typically <100% IACS despite their bi-continuous network, likely implies that electrical properties are very sensitive to residual chemical impurities within Cu or Gr, as well as at Cu—Gr interfaces. These reports implicate the significance of achieving bi-continuous Cu-Gr networks, as well as high-quality graphene.

## 5. Theoretical Modeling and Simulation of Electronic Properties of Graphene-Based Materials

Here, our focus is on the theoretical framework for the electrical structures of the Gr and simple Cu-Gr systems, from quantum mechanics to molecular dynamics.

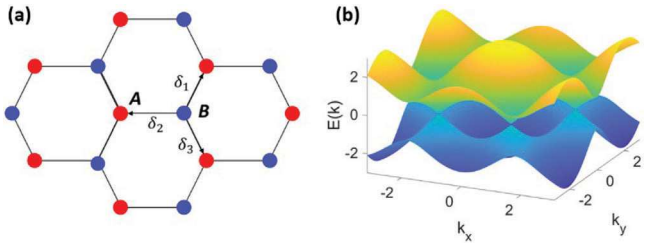


**Figure 13.** a) The honeycomb lattice structure of Gr. $\delta_i$, $i$ = 1, 2, and 3 are the nearest-neighbor vectors. b) The corresponding energy band structure of Gr in momentum space ($k_x$, $k_y$).

### 5.1. Single Layer Graphene

Gr is composed of carbon atoms arranged in a hexagonal structure, as shown in **Figure 13a**. The unit cell of lattice for Gr is made of two different types of atomic sites (i.e., A and B). The nearest-neighbor vectors are $\delta_1 = \frac{a}{2}(1, \sqrt{3})$, $\delta_2 = \frac{a}{2}(1, -\sqrt{3})$, and $\delta_2 = a(1, 0)$ where $a \approx 1.42$ Å, i.e., the carbon-carbon distance. By considering the nearest-neighbor hopping, the tight-binding Hamiltonian for Gr is described as:

$$\hat{H} = -t\sum_{\langle ij\rangle}\left(\hat{a}_i^{\dagger}\hat{b}_j + \hat{b}_j^{\dagger}\hat{a}_i\right) = -t\sum_{i\in A}\sum_{\delta}\left(\hat{a}_i^{\dagger}\hat{b}_{i+\delta} + \hat{b}_{i+\delta}^{\dagger}\hat{a}_i\right)$$

$$= -t\sum_{k}\begin{pmatrix}\hat{a}_k\\ \hat{b}_k\end{pmatrix}\begin{pmatrix}0 & \sum_{\delta}e^{ik\delta}\\ \sum_{\delta}e^{-ik\delta} & 0\end{pmatrix}\begin{pmatrix}\hat{a}_k^{\dagger} & b_k^{\dagger}\end{pmatrix} \quad (3)$$

where $t$ is the nearest-neighbor hopping energy, $i$ and $j$ are $A$ and $B$ sites, and $\hat{a}_i^{\dagger}$, $\hat{b}_j^{\dagger}$, $\hat{a}_i$, and $\hat{b}_i$ are the creation and annihilation operators for an electron at the $A$ site.[104] $\boldsymbol{k}$ represents a vector in the momentum space. The eigenvalues of the Hamiltonian matrix given in Equation (3) are $E_{\pm}(\boldsymbol{k}) = \pm t\sqrt{(3 + 4\cos(\frac{3}{2}k_x a)\cos(\frac{\sqrt{3}}{2}k_y a) + 2\cos(\sqrt{3}k_y a)}$. Figure 13b represents the energy band structure of Gr with the upper and lower band with the plus and minus signs for $t$, respectively. It is worth noting that when $\boldsymbol{k}$ is nearby the Dirac point $\mathbf{K} = \frac{2\pi}{3\sqrt{3}a}(\sqrt{3}, 1)$ or $\mathbf{K}' = \frac{2\pi}{3\sqrt{3}a}(\sqrt{3}, -1)$, the dispersion relation is $E_{\pm}(\mathbf{q}) = v_F|\mathbf{q}|$ where $\mathbf{q}$ is relatively smaller than magnitude of $\mathbf{K}$ or $\mathbf{K}'$ and $v_F$ is the Dirac-Fermi velocity, indicating linear in momentum space (so-called Dirac cone structure). The Dirac-cone structure of single layer Gr around the Fermi surface shows gapless semiconductor behavior, while multilayer Gr behaves as semimetal with extremely small band overlap.[105] Due to the linear dispersion relation, the effective mass of Gr is zero, resulting in unique electronic properties (e.g., remarkable electron mobility).[106]

### 5.2. Bilayer or Multilayer Graphene

When the number of Gr layers is more than one, successive layers are stacked in a way that atom $A$ is located directly above atom $B$ for bilayer Gr (i.e., Bernal or AB stacking), and the third layer is situated in the same direction again as the second one is stacked with respect to the first layer (i.e., rhombohedral or ABC stacking). Partoens et al. have evaluated the electronic structure change of 2, 3, and more layers of Gr, particularly around

the Dirac **K** point, based on a tight-binding approach.[105] In their study, the electronic structure of bilayer Gr represents a small band overlap between the conduction and valence band of 1.6 meV, and the band overlap for ≥ 3 layers of Gr is only 10% lower than that for graphite (41 meV), showing a semimetal behavior. Electronic properties that depend on the number of Gr layers have also been investigated.[107] The authors of this study developed a theoretical model of the electrical conductivity of multilayer Gr based on the Boltzmann transport equation and 2D electron gas theory by considering electron-electron and electron-phonon scattering. They found that the electrical resistivity ($\rho$) rapidly increases with increasing the number of layers from 2 ($\rho = 1.9\ \mu\Omega\ cm$) to 100 ($\rho = 147\ \mu\Omega\ cm$) layers. Beyond this, $\rho$ appears to slowly increase or plateau. Note that the resistivity of Gr consisting of ≥ 2 layers decreases as temperature increases, indicating a dominant transport channel changes from the surface to the interlayer of the Gr system. For theoretical studies of microscale or larger Gr systems, Rizzi et al. developed a network model of Gr-based conductor materials (GCMs),[108,109] e.g., to simulate randomly distributed Gr flakes. Interestingly, their model shows that the Gr's packing density (i.e., the amount of Gr flakes per unit volume) and its in-plane conductivity decide the total conductivity of the system, while a Gr flake's size governs how fast a given system reaches the maximum electrical conductivity as a function of an out-of-plane conductivity of the Gr flake.

### 5.3. Graphene-Copper Composite

As reviewed above, the Fermi energy of a freestanding Gr film is located at the conical points. However, Gr structures on a metallic substrate are significantly influenced by Gr-metal interfacial interplays. Therefore, it is very important to understand how metal atoms interact with Gr in the scope of electrical responses of CGCs. Depending on the binding energy, the metal-Gr interplay can be divided into two types: 1) physisorbed (i.e., weak interfacial bonding) for Al, Cu, Ag, Au, and Pt and 2) chemisorbed (i.e., strong interfacial bonding) for Co, Ni, Pd, and Ti.[110–113] For clarification, the emphasis of this section is on the physisorbed bond, as it is relevant to the Cu—Gr interaction.

First-principles calculations with density functional theory (DFT)[111,112,114] have been commonly utilized to investigate the bonding formation and electronic structure at a Cu-Gr contact. For example, Giovannetti et al. have studied the adsorption of Gr on Cu(111) surfaces.[111] Their study has found that an equilibrium Cu-Gr separation ($d_{eq} = 3.26$ Å) is considerably larger than that of chemisorbed Gr-metal bonding (e.g., $d_{eq}$ (Ni-G) = 2.05 Å). The Cu-Gr interaction is intrinsically weak due to the fully filled 3*d* orbital of Cu and, as a result, the electronic band structure of Gr mostly preserves its intrinsic characteristics in the CGC systems. Moreover, the Fermi energy downshift, $\Delta E_F = -0.22$ eV (i.e., n-type doping), from conical points for the absorbed Gr is found by comparing the work functions of Gr and Cu. Note that other computational studies on Cu—Gr have reported qualitatively similar conclusions but with different quantitative predictions, e.g., $d_{eq} = 3.46$ Å and $\Delta E_F = -0.06$ eV.[114] In contrast, it is known that much stronger chemisorbed bonds can alter the band structures of both Gr and metal,[112,114] e.g., the Ti-G interface forms strong covalence bonds between Ti's *d*- orbitals and the Gr's $p_z$-orbitals and reduces contact resistance.

The Cu-Gr interaction, although it is weak, affects the electronic behavior of the Cu—Gr systems. Many existing computational studies of the Cu—Gr system mainly focusing on its contact resistance in the scope of electronic applications are indeed available in the literature. Maassen et al. have studied the electronic properties of Cu—Gr interface by considering free-stranding pristine Gr connected to the Cu—Gr—Cu lead structure, as shown in **Figure 14a**.[115] By applying bias voltage on the right lead, they found a distinctive peak in the differential conductance ($dI/dV$) ≈− 0.63 V, which is not observed in pure Gr. Liu et al. have additionally investigated the molecular orbital symmetry effect on armchair Gr nanoribbon (AGN) deposited on a Cu(111) surface[116] (see Figure 14b). This suggests that the interaction between Gr and Cu *s* orbitals gives rise to limited electron transmission through the Cu—Gr interface and, therefore, higher Cu-Gr contact resistance. Ji et al. further studied Cu—Gr contact resistance[117] and found that it is directional, i.e., the total and lateral resistances of the Cu-Gr system are 627 and 295 Ω μ*m*, respectivtly. The authors argued that Gr in CGCs retains its conical electronic structure due to the weak Cu—Gr interaction and, as a result, lateral electron transport is effective compared to tunneling efficiency through the Cu—Gr interface. Because of this directional electron transport, aligning Gr structures in CGCs with the direction of electrical current becomes relevant.

## 6. Other Advantages of CGC Conductors

### 6.1. Charge Carrying Capacity

Each conductor has its own charge-carrying capacity (or ampacity limit) mainly associated with its thermal-electrical coupling behavior, i.e., excessive joule heating from the electrical current. A common metal conductor, when subjected to high temperatures, becomes more resistive to electrical current and more reactive to ambient gases, and, as a result, fails to sustain its conductivity and even its structural shape. The ampacity limit of a conductor depends on both its electrical and thermal conductivities to decrease joule heating and increase thermal dissipation, respectively. Owing to Gr's outstanding in-plane thermal conductivity[118] and thermal stability,[119] several CGCs have demonstrated significant improvement in ampacity limit.

One common approach is based on a CGC wire consisting of a Cu core and a Gr shell (or vice versa),[34,72,79,81,102] as shown in **Figure 15a,c**, respectively. Note that Cu and Gr, axially aligned in the electrical current direction, form parallel electrical paths. Each CGC study reported 4.5 times [34] and ten times [79] higher ampacity limits compared to a pure Cu wire. Despite their structural similarity, each study also presents different advantages depending on the status and quantity of Gr in each CGC wire. For example, fine Cu wires coated by high-quality CVD-grown Gr (called ACGC) offer higher electrical conductivity (123.8% IACS),[34] while a Gr yarn[79] coated by a Cu shell achieves lower density and higher thermal conductivity mainly due to a larger Gr-to-Cu volume fraction.

In light of recent progress in CGC wires, the concept of the axially continuous core–shell wires has been explored further to attain CGCs with even better electrical conductivity or

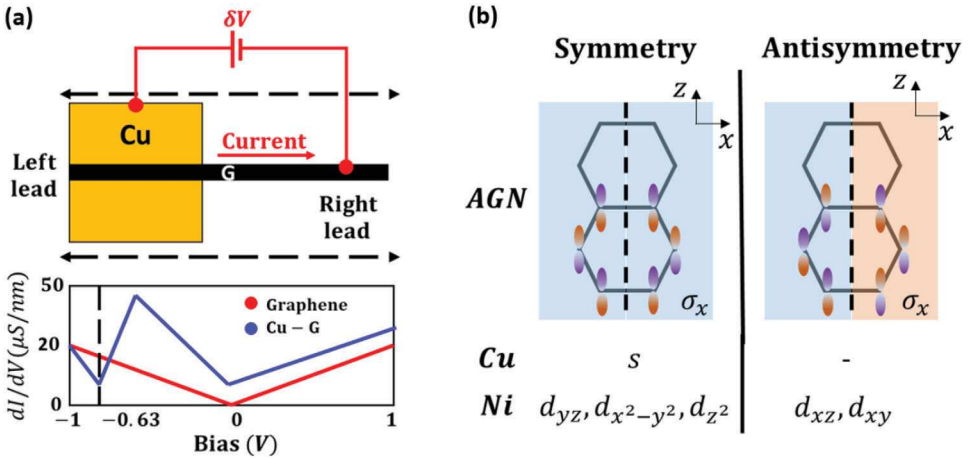


**Figure 14.** a) A schematic diagram of a Cu-Gr interface with the left and right leads (i.e., Cu contacted with Gr and pure Gr) by applying a bias voltage ($\delta V$) (top). Differential conductance ($dI/dV$) of pristine Gr (red) and Cu—Gr (blue) as a function of bias voltage ($V$) (bottom).[115] b) Molecular orbitals of armchair Gr nanoribbon (AGN), Cu, and nickel (Ni) with respect to the $\sigma_x$ plane. The left and right columns represent symmetric and antisymmetric orbital lists.[116]

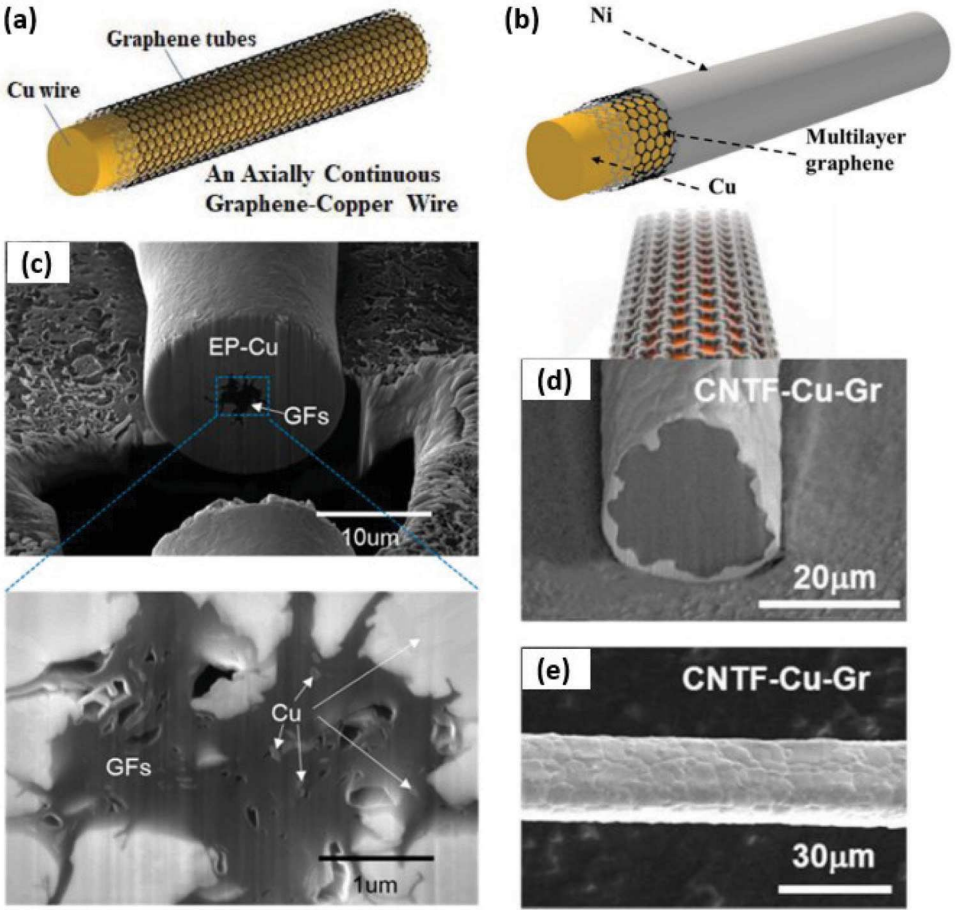


**Figure 15.** Schematic and SEM images of CGC wires of high ampacity. a) A schematic of the ACGC wire.[34] b) A schematic of the Gr-coated Cu wire after Ni deposition (NiGCu).[102] c) Cross-sectional SEM images of electroplated Cu on CVD-Gr fiber (EP Cu-GFs).[79] d) Cross-sectional SEM image of carbon nanotube fibers with core–shell structure of Cu deposition and CVD Gr coating (a CNTF-Cu-Gr wire). e) An SEM image of the CNTF-Cu-Gr wire.[81] c) reprinted (adapted) with permission from.[79] Copyright 2018 American Chemical Society. (a) is reproduced with permission.[34] Copyright 2021, John Wiley and Sons. (b) is reproduced with permission.[102] Copyright 2023, John Wiley and Sons. d,e) are reproduced with permission.[81] Copyright 2021, Elsevier.

additional functionality. Figure 15b[102] offers a schematic of a Cu wire coated by Gr and Ni layers (i.e., NiGCu). For fabrication, Gr was first grown on a Cu wire by CVD and then Ni was deposited onto the Gr surface. Because the outermost Ni shell protects the embedded Gr layer against oxidation at high temperatures, the NiGCu composite wire has oxidation resistance up to 650 °C, as well as a 61.2% higher ampacity limit compared to Cu. Another example, shown in Figure 15d,e, is a carbon nanotube fiber coated by Cu and Gr layers (referred to as CNTF-Cu—Gr). The fabrication flow was the deposition of Cu onto a carbon nanotube fiber followed by CVD Gr growth on Cu. The volume fraction of a carbon fiber increased significantly, thus a light-weight wire was obtained with a higher specific ampacity ($4.42 \times 10^4 \mathrm{A}\ \frac{cm}{g}$) than the controlled samples, including bare CNTF, CNTF-Cu, and annealed CNTF-Cu wires (see Figure 15 for details). Unfortunately, because of the deteriorated Gr property of the large core, the absolute values of ampacity and electrical conductivities were not as good as Cu.[81] Using these results, it can be speculated that increasing the Gr volume fraction with high-quality Gr would be one of the directions to achieve further improvement of ampacity. Of course, the successful development of a new conductor with an ultrahigh high-power transmission capability would be directly relevant to emerging technologies in the electric vehicle and semiconductor industries.

### 6.2. Thermal and Chemical Robustness

Cu is chemically active under ambient conditions and, thus, is not readily renewable. Because of this, a pure Cu conductor has a limited lifespan and often requires expensive maintenance and a protective layer, especially in harsh environments. Gr is well known for its thermal stability and chemical inertness, showing great potential for protective coating applications.[120–122] In addition, carbons in Gr are tightly packed with a short carbon-carbon bond length (0.142 nm),[123] smaller than the Van der Waals radius of a carbon atom (0.17 nm).[124] This unique 2D atomic structure makes Gr impermeable even to the smallest molecules, such as hydrogen.[125] Considering these attributes, Gr is an excellent option as a protective diffusion barrier in a wide range of thermally and chemically harsh conditions.[31,34,102] Here, we highlight a few studies that achieve Gr-enhanced resistance against material degradation of CGCs.

**Figure 16a,b**[31] shows examples of the enhanced anti-corrosion behavior of different CGC systems under chemically corrosive environments. The far-left image in Figure 16a shows a petri dish with a yellow etchant (0.5 wt.% $FeCl_3$) solution before adding (upper row) Gr-coated Cu powders or (lower row) bare Cu powders for corrosion tests. The color of the etchant remains unchanged for Gr-coated Cu powders, unlike bare Cu powders, after the same etching time (i.e., 90 s). These different observations qualitatively indicate a significantly reduced chemical reaction of Cu when protected by Gr. To facilitate this advantage, CGC with a so-called "brick-and-mortar" structure was fabricated by utilizing flake powder metallurgy of Gr-coated Cu powders. Because of its anisotropic structure (see Figure 16b), the corrosion rates of the CGC in Gr/Cu in-plane (Gr/Cu-ip) surface and Gr/Cu cross-plane (Gr/Cu-cp) surface (see inset in Figure 9b) were considerably different (0.289 and 0.210 mm/year, respectively), and were slower than the 0.316 mm/year for pure Cu. The authors argued that reactive molecules (e.g., oxygen, water) can diffuse through defects in Gr and then migrate mainly along the loosely packed Cu-Gr interfaces (see Figure 16b), explaining different corrosion depths in the Cr/Cu-cp and -ip directions. This study suggests that different architectures of Cu—Gr network can also influence the directional diffusion behavior of CGCs.

Figure 16c,d (from[34] and,[102] respectively) demonstrate the anti-oxidation performances of two different types of CGC wires (ACGC and NiGCu, respectively) under elevated temperatures. The electrical resistivity of 10-µm-diameter ACGC (or simply ACGC10) mostly preserved its original value, while that of the pure Cu counterpart (or simply A-Cu10) increased by 41.2% due to thermal oxidation (see the temperature profile (black solid line) in Figure 16c). 25-µm-diameter NiGCu wires in Figure 16d showed the electrical resistivity of 22.2 Ω nm after heat treatment, 56% improved compared to the pure metal composite wires without embedded Gr. The authors attributed the enhanced material performance of NiGCu to the impermeability of the embedded Gr layer that maintains a sharp Ni-Cu interface even at high temperatures.

In conclusion, Cu appropriately protected by impermeable Gr can maintain its electrical conductivity even under extreme conditions. Many CGCs have taken advantage of Gr and achieved their significantly improved anti-degradation properties under different corrosion/oxidation test conditions over a short- to intermediate-time period (e.g., 90 s in etchant and 144 h in neutral salt spray;[31] 2–24 h under elevated temperature[34,102] and up to 10 months in ambient air condition under room temperature).[34] Despite these technical advances, careful and innovative CGC designs are still crucial to avoid the negative effects of electrochemical reactions on CGC performance because defects in Gr structures can accelerate the corrosion of a metal surface.[126] Therefore, more studies are needed on the long-term protective functionality of Gr,[126] e.g., in the scope of CGCs over the years.

## 7. Applications and Future Perspectives

Improving the electrical performance of Cu, by fully exploiting the superb advantages of Gr, is directly relevant to reducing electrical energy loss by joule heating, transmitting higher current, and more effectively generating mechanical power from electrical motors. After two decades of research, the electrical performance of well-designed CGCs starts to exceed that of pure metal conductors, such as Cu and silver. The main mechanisms of the Gr-enhanced CGC conductivity are generally explained by reduced electron scattering at Gr-coated Cu surfaces, excellent electrical properties of continuous Gr, as well as thermally induced microstructural changes of a Cu matrix. Additionally, Gr acts as an effective diffusion barrier, blocking oxygen and other reactive chemicals and protecting Cu.

Our review clearly indicates that the electrical properties of CGCs depend on the Gr quality, Gr content, and continuity of both Gr and Cu networks in CGCs, emphasizing the importance of CGC manufacturing processes, including synthesis, dispersion, and consolidation. The current CGC technologies produce various forms of CGCs, e.g., wires, foils, meshes, and foams. This versatility of CGCs is crucial for different electrical

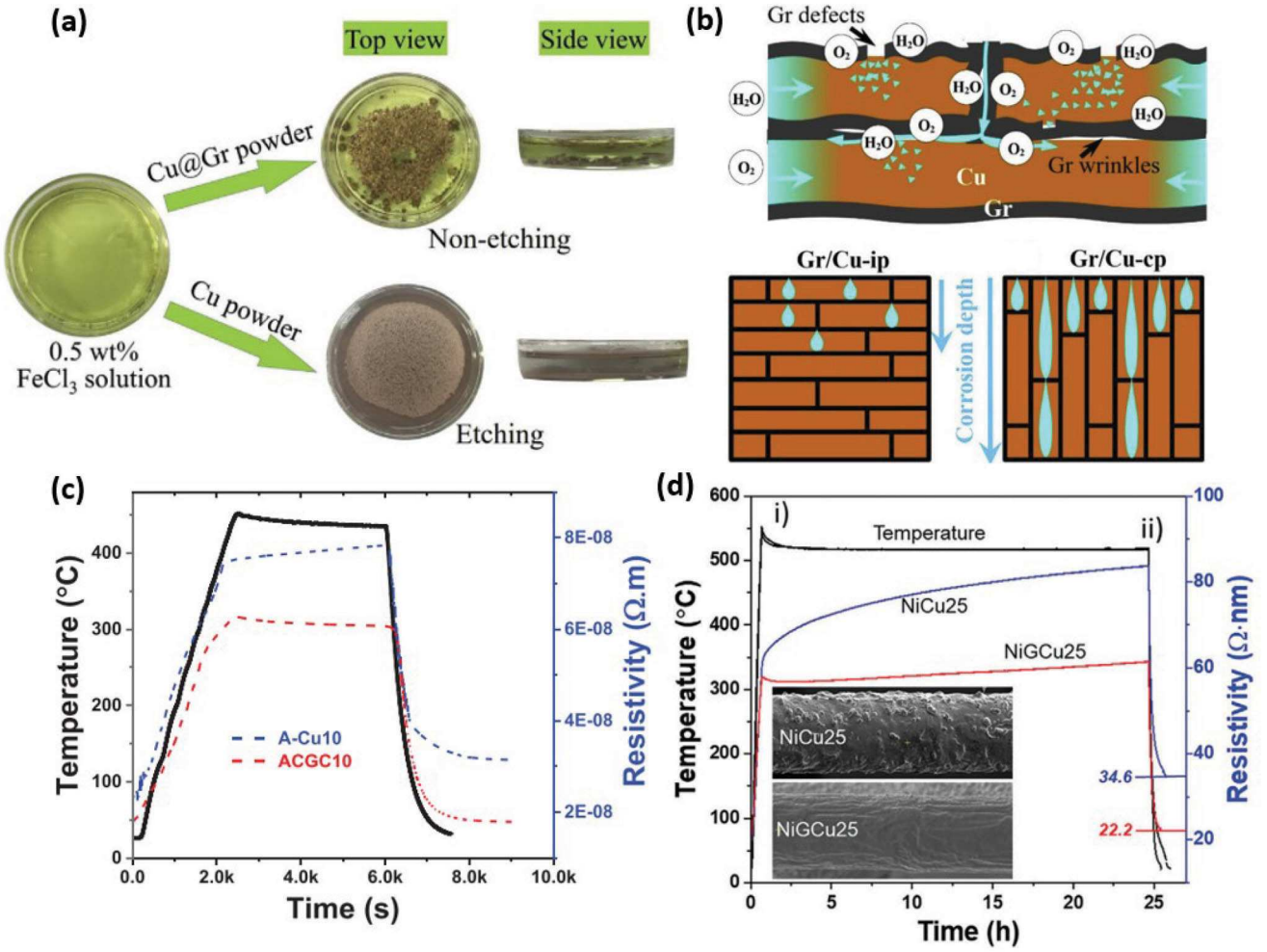


**Figure 16.** Antidegradation performances of CGCs. a) Comparison on corrosion behaviors of the pure Cu flakes and the CGC flakes in 0.5 wt.% $FeCl_3$ aqueous solution and b) schematic illustration for the possible pathway in the bulk CGC assembled from Cu@Gr nanoflakes. Gr/Cu in-plane (Gr/Cu-ip) surface and Gr/Cu cross-plane (Gr/Cu-cp) surface have different corrosion depth and rate because of Gr protected or exposed Cu matrix.[31] c) The temperature-dependent electrical resistivity of the annealed Cu (A—Cu) and ACGC wires (diameter = 10 μm).[34] d) The temperature-dependent electrical resistivity of the Ni-Cu wire (NiCu25) and Ni-Gr-Cu (NiGCu25) wires (diameter = 25 μm) under 24 h thermal annealing at 550 °C. In both (c) and (d), the temperature and resistivity measurements are synchronized in time and given using the vertical axes on the left and right, respectively.[102] (a) and (b) are reproduced with permission.[31] Copyright 2019, Elsevier. (c) is reproduced with permission.[34] Copyright 2021, John Wiley and Sons. (d) is reproduced with permission.[102] Copyright 2023, John Wiley and Sons.

applications, from high-power wire bonding in portable devices and charge collectors in batteries to larger-scale electrical motors and power grids. In the scope of effective power transmission, a few CGC wires are worth noting. Microscale fine Cu wires uniformly coated by CVD-grown Gr i.e., ACGC wire,[34] achieved a 450% increase in the current density breakdown limit, 41.2% lower resistivity, and a 224% higher heat dissipation compared to pure Cu. Another type of CGC wire consists of a Gr yarn coated by a thin Cu shell.[79] This work demonstrates a tenfold increase in the current density limit. To explore potential industrialized synthesis techniques, an ambient roll-to-roll CVD process[127] has been considered for high-throughput manufacturing of CGC wires.

Recent studies have shown that CGC conductors also achieve excellent mechanical strength and chemical robustness beyond bulk-scale pure Cu counterparts. This becomes very desirable when the conductors need to tolerate mechanical abrasion.[50,128–130] Additionally, the chemical stability of CGCs can potentially broaden their applications in a corrosive environment and/or elevated temperature, including lithium-ion batteries and car engines.[131,132] For instance, the corrosion current of a Gr-coated Cu sample was 20 times lower compared to pristine Cu.[133]

In addition to the conventional applications, CGC technologies may give rise to emerging applications, including wearable devices,[134–136] solar cells,[137,138] sensors,[139] and biological tools.[140,141] Owing to their superb electromagnetic shielding, CGCs can improve the reliability and robustness of wearable devices and sensors,[82] even in electromagnetically noisy environments. Furthermore, CGCs can also be utilized in supercapacitors[142–144] and energy storage devices.[145,146] For example, it has been shown that the use of a Gr-modified Cu foil as

the anode current collector reduces contact resistance and improves the discharge capacity and cycle life of the lithium-ion battery.[147]

Despite the remarkable technical advances in CGCs, there are still remaining challenges in the field. First, cost-effective high-throughput manufacturing of high-quality CGCs must be achieved for their practical application. During the development of new manufacturing methods, several aspects must be appropriately considered: 1) Optimization of Gr growth, including homogeneous dispersion of Gr, precise control on the number of layers and quality of Gr, and orientational alignments of intrinsically planar Gr structures; 2) Mechanisms of Cu-Gr interactions in the scope of improving electrical properties of CGCs; 3) Adaption of industry-scale production techniques of CGCs, e.g., roll-to-roll manufacturing. Another interesting research direction is to engineer CGCs with additional functionality. For example, new CGC-based conductors, by utilizing thermal stability, chemical inertness, and mechanical strength of Gr, can be used in extremely harsh conditions, e.g., extremely high current, high temperature, mechanical stress, and corrosive environments, for innovative electric vehicle, aerospace, and battery applications.

## Acknowledgements

This project was supported by the Office of Naval Research (N00014-22-1-2146 and N00014-23-1-2388) and the National Science Foundation (CMMI-23–38609). The authors thank Dr. Zhizhong Chen for valuable discussions and comments.

## Conflict of Interest

The authors declare no conflict of interest.

## Keywords

ampacity, anti-corrosion, composite, conductor, copper, electrical conductivity, graphene

Received: April 22, 2024
Revised: June 6, 2024
Published online:

[1] S. W. Stratton, *Circular of the Bureau of Standards*, 1st ed., NIST, Gaithersburg, MD **1912**, p. 67.
[2] U.S. Energy Information Administration, Electricity Data Browser, https://www.eia.gov (accessed: February 2024).
[3] 100% Carbon Pollution-Free Electricity on a Net Annual Basis by 2030, Including 50% on a 24/7 Basis, https://www.sustainability.gov/federalsustainabilityplan/carbon.html (accessed: February 2024).
[4] *Efficient Electrical Energy Transmission and Distribution*, IEC, Geneva 20, Switzerland **2007**, p. 24.
[5] R. Saidur, *Renew. Sustain. Energy Rev.* **2010**, *14*, 877.
[6] K. S. Novoselov, A. K. Geim, S. V. Morozov, D. Jiang, Y. Zhang, S. V. Dubonos, I. V. Grigorieva, A. A. Firsov, *Science* **2004**, *306*, 666.
[7] K. I. Bolotin, K. J. Sikes, Z. Jiang, M. Klima, G. Fudenberg, J. Hone, P. Kim, H. L. Stormer, *Solid State Commun.* **2008**, *146*, 351.
[8] A. A. Balandin, *Nat. Mater.* **2011**, *10*, 569.
[9] R. Murali, Y. Yang, K. Brenner, T. Beck, J. D. Meindl, *Appl. Phys. Lett.* **2009**, *94*, 243114.
[10] K. S. Novoselov, A. K. Geim, S. V. Morozov, D. Jiang, M. I. Katsnelson, I. V. Grigorieva, S. V. Dubonos, A. A. Firsov, *Nature* **2005**, *438*, 197.
[11] D. R. Slocombe, V. L. Kuznetsov, W. Grochala, R. J. Williams, P. P. Edwards, *Philos. Trans. A Math. Phys. Eng. Sci.* **2015**, *373*, 20140476.
[12] J.-H. Chen, C. Jang, S. Xiao, M. Ishigami, M. S. Fuhrer, *Nat. Nanotechnol.* **2008**, *3*, 206.
[13] W. M. Haynes, *CRC Handbook of Chemistry and Physics*, CRC Press, Boca Raton, FL **2014**.
[14] K. I. Bolotin, K. Sikes, Z. Jiang, M. Klima, G. Fudenberg, J. Hone, P. Kim, H. L. Stormer, *Solid State Commun.* **2008**, *146*, 351.
[15] R. W. Chabay, B. A. Sherwood, *Matter and Interactions*, Vol. *2*, 4th ed., John Wiley & Sons, Hoboken NJ **2018**.
[16] L. Banszerus, M. Schmitz, S. Engels, M. Goldsche, K. Watanabe, T. Taniguchi, B. Beschoten, C. Stampfer, *Nano Lett.* **2016**, *16*, 1387.
[17] S. Debroy, S. Sivasubramani, G. Vaidya, S. G. Acharyya, A. Acharyya, *Sci. Rep.* **2020**, *10*, 6240.
[18] A. A. Balandin, S. Ghosh, W. Bao, I. Calizo, D. Teweldebrhan, F. Miao, C. N. Lau, *Nano Lett.* **2008**, *8*, 902.
[19] D. Yoon, Y.-W. Son, H. Cheong, *Nano Lett.* **2011**, *11*, 3227.
[20] E. Pop, V. Varshney, A. K. Roy, *MRS Bull.* **2012**, *37*, 1273.
[21] J.-W. Jiang, J.-S. Wang, B. Li, *Phys. Rev. B* **2009**, *80*, 113405.
[22] H. Ledbetter, E. Naimon, *J. Phys. Chem. Ref. Data* **1974**, *3*, 897.
[23] C. Lee, X. Wei, J. W. Kysar, J. Hone, *Science* **2008**, *321*, 385.
[24] R. Peierls,*Ann. I. H. Poincare* **1935**, *5*, 177.
[25] K. S. Novoselov, A. K. Geim, S. V. Morozov, D. Jiang, M. I. Katsnelson, I. V. Grigorieva, S. Dubonos, A. A. Firsov, *Nature* **2005**, *438*, 197.
[26] X. Du, I. Skachko, A. Barker, E. Y. Andrei, *Nat. Nanotechnol.* **2008**, *3*, 491.
[27] S. Pei, H.-M. Cheng, *Carbon* **2012**, *50*, 3210.
[28] C. K. Chua, M. Pumera, *Chem. Soc. Rev.* **2014**, *43*, 291.
[29] X. Zhang, Y. Xu, M. Wang, E. Liu, N. Zhao, C. Shi, D. Lin, F. Zhu, C. He, *Nat. Commun.* **2020**, *11*, 2775.
[30] C. Mattevi, H. Kim, M. Chhowalla, *J. Mater. Chem.* **2011**, *21*, 3324.
[31] B. Jin, D.-B. Xiong, Z. Tan, G. Fan, Q. Guo, Y. Su, Z. Li, D. Zhang, *Carbon* **2019**, *142*, 482.
[32] M. Cao, D. B. Xiong, L. Yang, S. Li, Y. Xie, Q. Guo, Z. Li, H. Adams, J. Gu, T. Fan, *Adv. Funct. Mater.* **2019**, *29*, 1806792.
[33] T. Li, Y. Wang, M. Yang, H. Hou, S. Wu, *J. Alloys Compd.* **2021**, *851*, 156703.
[34] H. Kashani, C. Kim, C. Rudolf, F. K. Perkins, E. R. Cleveland, W. Kang, *Adv. Mater.* **2021**, *33*, 2104208.
[35] J. Yang, Y. He, X. Zhang, W. Yang, Y. Li, X. Li, Q. Chen, X. Chen, K. Du, Y. Yan, *J. Mater. Res. Technol.* **2021**, *15*, 3005.
[36] K. S. Kappagantula, J. A. Smith, A. K. Nittala, F. F. Kraft, *J. Alloys Compd.* **2022**, *894*, 162477.
[37] X. Liu, Y. Huang, L. Wu, R. Liu, Y. Li, Q. Chen, *ACS Appl. Nano Mater.* **2023**, *6*, 2697.
[38] M. Cao, D.-B. Xiong, Z. Tan, G. Ji, B. Amin-Ahmadi, Q. Guo, G. Fan, C. Guo, Z. Li, D. Zhang, *Carbon* **2017**, *117*, 65.
[39] Z. Yang, L. Wang, J. Li, Z. Shi, M. Wang, J. Sheng, W. Fei, *Mater. Sci. Eng., A* **2021**, *820*, 141579.
[40] C. Salvo, R. Mangalaraja, R. Udayabashkar, M. Lopez, C. Aguilar, *J. Alloys Compd.* **2019**, *777*, 309.
[41] G. Singh, P. M. Pandey, *Rapid Prototyping J.* **2020**, *26*, 765.
[42] Z. Yang, L. Wang, Z. Shi, M. Wang, Y. Cui, B. Wei, S. Xu, Y. Zhu, W. Fei, *Carbon* **2018**, *127*, 329.
[43] M. Tabandeh-Khorshid, A. Kumar, E. Omrani, C. Kim, P. Rohatgi, *Composites, Part B* **2020**, *183*, 107664.
[44] X. Zhang, N. Zhao, C. He, *Prog. Mater. Sci.* **2020**, *113*, 100672.

 

[45] Ö. Güler, N. Bağcı, *J. Mater. Res. Technol.* **2020**, *9*, 6808.
[46] P. Hidalgo-Manrique, X. Lei, R. Xu, M. Zhou, I. A. Kinloch, R. J. Young, *J. Mater. Sci.* **2019**, *54*, 12236.
[47] M. Tehrani, *Physica Status Solidi* **2021**, *218*, 2000704.
[48] R. T. Mathew, S. Singam, P. Kollu, S. Bohm, M. Prasad, *J. Alloys Compd.* **2020**, *840*, 155725.
[49] F. Chen, Q. Mei, J. Li, C. Li, L. Wan, G. Zhang, X. Mei, Z. Chen, T. Xu, Y. Wang, *Composites, Part B* **2021**, *216*, 108850.
[50] N. Khobragade, K. Sikdar, B. Kumar, S. Bera, D. Roy, *J. Alloys Compd.* **2019**, *776*, 123.
[51] H. Asgharzadeh, S. Eslami, *J. Alloys Compd.* **2019**, *806*, 553.
[52] P. Vázquez-Sánchez, M. Rodríguez-Escudero, F. Burgos, I. Llorente, O. Caballero-Calero, M. M. González, R. Fernández, M. García-Alonso, *J. Alloys Compd.* **2019**, *800*, 379.
[53] T. Yang, W. Chen, F. Yan, H. Lv, Y. Q. Fu, *Vacuum* **2021**, *183*, 109861.
[54] G. Shao, P. Liu, W. Li, X. Chen, F. Ma, X. Liu, H. Zhou, K. Zhang, *J. Alloys Compd.* **2020**, *829*, 154356.
[55] J. Yu, L. Wang, Z. Liu, J. Xu, Y. Zong, *J. Alloys Compd.* **2022**, *924*, 166610.
[56] Y. Yang, Y. Liang, G. He, P. Luo, *Mater. Sci. Eng., A* **2022**, *847*, 143349.
[57] A. Yan, H. Jiang, J. Yu, Q. Zhao, Z. Wu, J. Tao, C. Li, J. Yi, Y. Liu, *Mater. Sci. Eng., A* **2023**, *867*, 144500.
[58] R. Ma, Y. He, L. Liu, R. Bao, J. Yi, J. Tao, C. Li, X. Mu, *Vacuum* **2023**, *211*, 111964.
[59] X. Li, S. Yan, X. Chen, Q. Hong, N. Wang, *J. Alloys Compd.* **2020**, *834*, 155182.
[60] T. Zuo, J. Xue, Y. Ru, Z. Gao, L. Zhang, B. Da, L. Han, L. Xiao, *Mater. Lett.* **2021**, *283*, 128895.
[61] M. Wang, J. Sheng, L.-D. Wang, G. Wang, W.-D. Fei, *J. Mater. Res. Technol.* **2022**, *17*, 3205.
[62] Z. Gao, T. Zuo, M. Wang, L. Zhang, B. Da, Y. Ru, J. Xue, Y. Wu, L. Han, L. Xiao, *Carbon* **2022**, *186*, 303.
[63] M. Wang, T. Zuo, J. Xue, Y. Ru, Y. Wu, Z. Xu, Z. Gao, L. Han, L. Xiao, *Mater. Lett.* **2022**, *319*, 132219.
[64] T. Yang, W. Chen, H. Zhang, L. Ma, Y.-Q. Fu, *Mater. Sci. Eng., A* **2022**, *835*, 142662.
[65] T. Zuo, M. Wang, J. Xue, Y. Ru, L. Zhang, B. Da, Y. Wu, Z. Xu, Z. Gao, P. K. Liaw, *Carbon* **2022**, *197*, 455.
[66] T. Zuo, M. Wang, J. Xue, Y. Ru, Y. Wu, F. Ding, B. Da, Z. Xu, P. K. Liaw, Z. Gao, *Mater. Charact.* **2023**, *200*, 112863.
[67] L.-W. Jang, L. Zhang, M. Menghini, H. Cho, J. Y. Hwang, D. I. Son, J.-P. Locquet, J. W. Seo, *Carbon* **2018**, *139*, 666.
[68] S. Fu, X. Chen, P. Liu, *Mater. Sci. Eng., A* **2020**, *771*, 138656.
[69] T. Li, Y. Wang, M. Yang, H. Hou, S. Wu, *Mater. Sci. Eng., A* **2021**, *826*, 141983.
[70] S. Shu, Q. Yuan, W. Dai, M. Wu, D. Dai, K. Yang, B. Wang, C.-T. Lin, T. Wuebben, J. Degenhardt, *Mater. Des.* **2021**, *203*, 109586.
[71] R. Mehta, S. Chugh, Z. Chen, *Nano Lett.* **2015**, *15*, 2024.
[72] K. Zhao, T. Zhang, A. Ren, Y. Yang, P. Xiao, Z. Ge, Y. Ma, Y. Chen, *Carbon* **2019**, *141*, 198.
[73] Z. Dong, Y. Peng, X. Zhang, D.-B. Xiong, *Compos. Commun.* **2021**, *24*, 100619.
[74] K. Chu, F. Wang, X. Wang, D. Huang, *Mater. Sci. Eng., A* **2018**, *713*, 269.
[75] S. Huang, Q. Zhang, P. Li, F. Ren, A. Yurtsever, D. Ma, *Adv. Energy Mater.* **2018**, *8*, 1703658.
[76] K. Chu, F. Wang, Y. Li, X. Wang, D. Huang, Z. Geng, *Composites, Part A* **2018**, *109*, 267.
[77] R. B. Naik, K. V. Reddy, G. M. Reddy, R. A. Kumar, *Mater. Lett.* **2020**, *265*, 127437.
[78] R. Navik, D. Xiao, Y. Gai, H. Tan, Y. Zhao, *Appl. Surf. Sci.* **2020**, *527*, 146694.
[79] S. J. Kim, D. H. Shin, Y. S. Choi, H. Rho, M. Park, B. J. Moon, Y. Kim, S.-K. Lee, D. S. Lee, T.-W. Kim, *ACS Nano* **2018**, *12*, 2803.
[80] M. Li, K. Yang, W. Zhu, J. Shen, J. Rollinson, M. Hella, J. Lian, *ACS Appl. Nano Mater.* **2020**, *3*, 5565.
[81] M. Park, D.-M. Lee, M. Park, S. Park, D. S. Lee, T.-W. Kim, S. H. Lee, S.-K. Lee, H. S. Jeong, B. H. Hong, *Carbon* **2021**, *179*, 53.
[82] Z. Wang, B. Mao, Q. Wang, J. Yu, J. Dai, R. Song, Z. Pu, D. He, Z. Wu, S. Mu, *Small* **2018**, *14*, 1704332.
[83] J. Hwang, T. Yoon, S. H. Jin, J. Lee, T. S. Kim, S. H. Hong, S. Jeon, *Adv. Mater.* **2013**, *25*, 6724.
[84] F. Luo, X. Jiang, H. Sun, D. Mo, Y. Zhang, R. Shu, X. Li, *J. Alloys Compd.* **2022**, *925*, 166710.
[85] R. Jiang, X. Zhou, Q. Fang, Z. Liu, *Mater. Sci. Eng., A* **2016**, *654*, 124.
[86] Z. Qiao, T. Zhou, J. Kang, Z. Yu, G. Zhang, M. Li, H. Lu, Y. Li, Q. Huang, L. Wang, *Mater. Lett.* **2018**, *224*, 37.
[87] G. Xin, H. Sun, T. Hu, H. R. Fard, X. Sun, N. Koratkar, T. Borca-Tasciuc, J. Lian, *Adv. Mater.* **2014**, *26*, 4521.
[88] X. Dong, C.-Y. Su, W. Zhang, J. Zhao, Q. Ling, W. Huang, P. Chen, L.-J. Li, *Phys. Chem. Chem. Phys.* **2010**, *12*, 2164.
[89] J.-C. Charlier, X. Gonze, J.-P. Michenaud, *Europhys. Lett.* **1994**, *28*, 403.
[90] A. C. Ferrari, J. C. Meyer, V. Scardaci, C. Casiraghi, M. Lazzeri, F. Mauri, S. Piscanec, D. Jiang, K. S. Novoselov, S. Roth, *Phys. Rev. Lett.* **2006**, *97*, 187401.
[91] M. Mirzaee, C. Dehghanian, K. S. Bokati, *J. Electroanal. Chem.* **2018**, *813*, 152.
[92] Y. Liu, Y. Ying, Y. Mao, L. Gu, Y. Wang, X. Peng, *Nanoscale* **2013**, *5*, 9134.
[93] X.-Y. Fang, X.-X. Yu, H.-M. Zheng, H.-B. Jin, L. Wang, M.-S. Cao, *Phys. Lett. A* **2015**, *379*, 2245.
[94] X. Li, W. Cai, L. Colombo, R. S. Ruoff, *Nano Lett.* **2009**, *9*, 4268.
[95] X. Li, C. W. Magnuson, A. Venugopal, R. M. Tromp, J. B. Hannon, E. M. Vogel, L. Colombo, R. S. Ruoff, *J. Am. Chem. Soc.* **2011**, *133*, 2816.
[96] L. M. Malard, M. A. Pimenta, G. Dresselhaus, M. S. Dresselhaus, *Phys. Rep.* **2009**, *473*, 51.
[97] H. Wang, Z. Yao, G. S. Jung, Q. Song, M. Hempel, T. Palacios, G. Chen, M. J. Buehler, A. Aspuru-Guzik, J. Kong, *Matter* **2021**, *4*, 3339.
[98] W. Fang, A. L. Hsu, Y. Song, A. G. Birdwell, M. Amani, M. Dubey, M. S. Dresselhaus, T. Palacios, J. Kong, *ACS Nano* **2014**, *8*, 6491.
[99] R. M. Brick, *Structure and Properties of Engineering Materials*, McGraw-Hill, New York **1977**.
[100] C. Li, Y. Lu, J. Yan, W. Yu, R. Zhao, S. Du, K. Niu, *R. Soc. Open Sci.* **2021**, *8*, 202309.
[101] J. T. Black, R. A. Kohser, E. P. DeGarmo, *Materials and Processes in Manufacturing*, Wiley, Hoboken, NJ **2003**.
[102] H. Kashani, W. J. Choi, C. Kim, R. Berlia, J. Rajagopalan, W. Kang, *Adv. Funct. Mater.* **2023**, *33*, 2214220.
[103] Z. Hashin, S. Shtrikman, *J. Appl. Phys.* **1962**, *33*, 3125.
[104] A. H. Castro Neto, F. Guinea, N. M. R. Peres, K. S. Novoselov, A. K. Geim, *Rev. Mod. Phys.* **2009**, *81*, 109.
[105] B. Partoens, F. M. Peeters, *Phys. Rev. B* **2006**, *74*, 075404.
[106] A. K. Geim, K. S. Novoselov, *Nat. Mater.* **2007**, *6*, 183.
[107] X.-Y. Fang, X.-X. Yu, H.-M. Zheng, H.-B. Jin, L. Wang, M.-S. Cao, *Phys. Lett. A* **2015**, *379*, 2245.
[108] L. Rizzi, A. Zienert, J. Schuster, M. Köhne, S. E. Schulz, *ACS Appl. Mater. Interfaces* **2018**, *10*, 43088.
[109] L. Rizzi, A. Zienert, J. Schuster, M. Köhne, S. E. Schulz, *Comput. Mater. Sci.* **2019**, *161*, 364.
[110] Y. Matsuda, W.-Q. Deng, W. A. Goddard, *J. Phys. Chem. C* **2007**, *111*, 11113.
[111] G. Giovannetti, P. A. Khomyakov, G. Brocks, V. M. Karpan, J. van den Brink, P. J. Kelly, *Phys. Rev. Lett.* **2008**, *101*, 026803.
[112] P. A. Khomyakov, G. Giovannetti, P. C. Rusu, G. Brocks, J. van den Brink, P. J. Kelly, *Phys. Rev. B* **2009**, *79*, 195425.

[113] C. Gong, G. Lee, B. Shan, E. M. Vogel, R. M. Wallace, K. Cho, *J. Appl. Phys.* **2010**, *108*, 123711.
[114] Q. Ran, M. Gao, X. Guan, Y. Wang, Z. Yu, *Appl. Phys. Lett.* **2009**, *94*, 103511.
[115] J. Maassen, W. Ji, H. Guo, *Appl. Phys. Lett.* **2010**, *97*, 142105.
[116] H. Liu, H. Kondo, T. Ohno, *Phys. Rev. B* **2012**, *86*, 155434.
[117] X. Ji, J. Zhang, Y. Wang, H. Qian, Z. Yu, *Phys. Chem. Chem. Phys.* **2013**, *15*, 17883.
[118] S. Ghosh, I. Calizo, D. Teweldebrhan, E. P. Pokatilov, D. L. Nika, A. A. Balandin, W. Bao, F. Miao, C. N. Lau, *Appl. Phys. Lett.* **2008**, *92*, 151911.
[119] H. Y. Nan, Z. H. Ni, J. Wang, Z. Zafar, Z. X. Shi, Y. Y. Wang, *J. Raman Spectrosc.* **2013**, *44*, 1018.
[120] D. Prasai, J. C. Tuberquia, R. R. Harl, G. K. Jennings, K. I. Bolotin, *ACS Nano* **2012**, *6*, 1102.
[121] R. S. Raman, P. C. Banerjee, D. E. Lobo, H. Gullapalli, M. Sumandasa, A. Kumar, L. Choudhary, R. Tkacz, P. M. Ajayan, M. Majumder, *Carbon* **2012**, *50*, 4040.
[122] F. Zhou, Z. Li, G. J. Shenoy, L. Li, H. Liu, *ACS Nano* **2013**, *7*, 6939.
[123] P. Trucano, R. Chen, *Nature* **1975**, *258*, 136.
[124] S. S. Batsanov, *Inorg. Mater.* **2001**, *37*, 871.
[125] M. H. Khan, M. Moradi, M. Dakhchoune, M. Rezaei, S. Huang, J. Zhao, K. V. Agrawal, *Carbon* **2019**, *153*, 458.
[126] M. Schriver, W. Regan, W. J. Gannett, A. M. Zaniewski, M. F. Crommie, A. Zettl, *ACS Nano* **2013**, *7*, 5763.
[127] N. Mishra, Y. Vlamidis, L. Martini, A. Lanza, Z. M. Gebeyehu, A. Jouvray, M. La Sala, M. Gemmi, V. Mišeikis, M. Perry, *ACS Appl. Engin. Mater.* **2023**, *1*, 1937.
[128] C. Sun, X. Zhang, N. Zhao, C. He, *Mater. Sci. Eng., A* **2019**, *756*, 82.
[129] L. Li, R. Sun, Y. Zhang, S. Kitipornchai, J. Yang, *Comput. Mater. Sci.* **2020**, *182*, 109759.
[130] W. Qu, J. Zhang, S. Zhang, N. Li, C. Liu, X. Yu, Y. Song, S. Han, L. Chen, M. Xi, *Compos. Commun.* **2022**, *32*, 101187.
[131] S. Chen, L. Brown, M. Levendorf, W. Cai, S.-Y. Ju, J. Edgeworth, X. Li, C. W. Magnuson, A. Velamakanni, R. D. Piner, *ACS Nano* **2011**, *5*, 1321.
[132] A. J. Datta, B. Gupta, M. Shafiei, R. Taylor, N. Motta, *Nanotechnology* **2016**, *27*, 285704.
[133] M. A. Krishnan, K. S. Aneja, A. Shaikh, S. Bohm, K. Sarkar, H. M. Bohm, V. Raja, *RSC Adv.* **2018**, *8*, 499.
[134] C. S. Yeo, H. Kim, T. Lim, H. J. Kim, S. Cho, K. R. Cho, Y. S. Kim, M. K. Shin, J. Yoo, S. Ju, *J. Mater. Chem. C* **2017**, *5*, 12825.
[135] P. Peng, L. Li, P. He, Y. Zhu, J. Fu, Y. Huang, W. Guo, *Nanotechnology* **2019**, *30*, 185301.
[136] A. Lamberti, A. Gigot, S. Bianco, M. Fontana, M. Castellino, E. Tresso, C. F. Pirri, *Carbon* **2016**, *105*, 649.
[137] Y. Ahn, Y. Jeong, D. Lee, Y. Lee, *ACS Nano* **2015**, *9*, 3125.
[138] H. Bi, H. Cui, T. Lin, F. Huang, *Carbon* **2015**, *91*, 153.
[139] Z. Li, S. Khuje, A. Chivate, Y. Huang, Y. Hu, L. An, Z. Shao, J. Wang, S. Chang, S. Ren, *ACS Appl. Electron. Mater.* **2020**, *2*, 1867.
[140] V. Vasilopoulos, M. Pitou, I. Fekas, R. Papi, A. Ouranidis, E. Pavlidou, P. Patsalas, T. Choli-Papadopoulou, *ACS Omega* **2020**, *5*, 26329.
[141] Y. Ouyang, X. Cai, Q. Shi, L. Liu, D. Wan, S. Tan, Y. Ouyang, *Colloids Surf., B* **2013**, *107*, 107.
[142] S. Chiam, H. Lim, S. Hafiz, A. Pandikumar, N. Huang, *Sci. Rep.* **2018**, *8*, 3093.
[143] H.-Y. Ho, H.-I. Chu, Y.-J. Huang, D.-S. Tsai, C.-P. Lee, *Nanotechnology* **2023**, *34*, 125401.
[144] M. Madito, K. Matshoba, F. U. Ochai-Ejeh, N. Mongwaketsi, C. Mtshali, M. Fabiane, N. Manyala, *Surf. Coat. Technol.* **2020**, *383*, 125230.
[145] Y. Fu, Q. Chen, M. He, Y. Wan, X. Sun, H. Xia, X. Wang, *Ind. Eng. Chem. Res.* **2012**, *51*, 11700.
[146] J. Zhao, R. Pan, R. Sun, C. Wen, S.-L. Zhang, B. Wu, L. Nyholm, Z.-B. Zhang, *Nano Energy* **2019**, *60*, 760.
[147] H. R. Kim, W. M. Choi, *Scr. Mater.* **2018**, *146*, 100.

**Jiali Yao** is a Ph.D. student under the supervision of Prof. Wonmo Kang at Arizona State University. She received her B.S. in Chemistry from the Chinese University of Hong Kong. Her research interests include graphene-metal composites for electrical applications and graphene-metal interplays.

**Chunghwan Kim** completed his Ph.D. at Arizona State University and is currently a postdoctoral researcher under the supervision of Prof. Wonmo Kang. His research focuses on the theoretical modeling of graphene-based composite systems for novel electrical and mechanical applications and the characterization of the dynamic behavior of soft biomaterials for blunt injury and wound healing mechanisms.

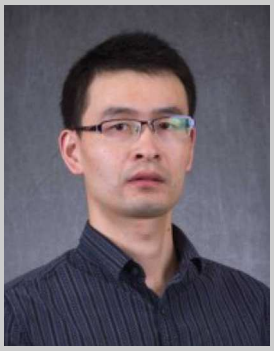

**Qiong Nian** is an Associate Professor of Aerospace and Mechanical Engineering and a graduate faculty of Materials Science and Engineering at the School for Engineering of Matter, Transport and Energy at Arizona State University. He received his B.S. degree from the University of Science & Technology of China, Hefei, China, in 2009 and his Ph.D. degree from Purdue University, West Lafayette, in 2015. His research interests include nanomanufacturing, additive manufacturing, laser-based material processing, laser-matter interaction, and physics simulation, inkjet printing of functional materials, 2D materials fabrication for energy storage, bio-sensors, and nanocomposites.

**Wonmo Kang** is an associate professor in the School for Engineering of Matter, Transport, and Energy at Arizona State University (ASU). He received his Ph.D. degree from the University of Illinois at Urbana-Champaign. Before joining ASU, he was a research scientist at the US Naval Research Laboratory. His current research includes graphene-metal composites for multifunctional applications, in situ material characterization, nano/bio-mechanics, and NEMS/MEMS/bioMEMS.